Laser powder bed fusion of metallic components: Latest progress in productivity, quality, and cost perspectives

Journal of Materials Research and Technology 27 (2023) 6484–6500

Contents lists available at ScienceDirect

Journal of Materials Research and Technology

journal homepage: www.elsevier.com/locate/jmrt

Laser powder bed fusion of metallic components: Latest progress in productivity, quality, and cost perspectives

Mohammad Taghian [a], Mohammad Hossein Mosallanejad [a,*], Erika Lannunziata [a], Giovanni Del Greco [b], Luca Iuliano [a], Abdollah Saboori [a,**]

[a] Integrated Additive Manufacturing Center, Department of Management and Production Engineering (DIGEP), Politecnico di Torino, Corso Duca Degli Abruzzi, 24, 10129, Torino, Italy

[b] Department of Mechanical and Aerospace Engineering, Politecnico di Torino, Corso Duca degli Abruzzi, 24, 10129, Torino, Italy

ARTICLE INFO

Keywords:
Additive manufacturing
Laser powder bed fusion
Productivity
Quality
Cost analysis

ABSTRACT

Laser Powder Bed Fusion (L-PBF) is an innovative metal Additive Manufacturing process that enables the production of highly complex parts with unique precision, making it a crucial technology for demanding applications such as aerospace and automotive industries. However, the efficiency of the L-PBF process should be enhanced compared to traditional manufacturing methods to approach alleviated production costs and improved productivity. This paper presents a comprehensive overview of the L-PBF process, including the primary factors that impact productivity and quality performance. Hence, several efforts have been undertaken to address these limitations and explore various innovative strategies. Modifications to process parameters, such as increasing the layer thickness and employing statistical approaches, optimization algorithms, and numerical modeling to advance the construction rate, are part of efforts to improve the efficacy of L-PBF. Considering the economic implications and practical implementation of these innovations alongside such approaches is essential. These factors are critical for ensuring that the advantages of increased productivity and decreased costs are realized across various applications. Through a series of illustrative case studies, this paper demonstrates how these approaches can improve the performance of L-PBF and help realize its full potential across an extensive range of applications.

1. Introduction

Additive Manufacturing (AM) processes offer the ability to produce complex but high-quality parts directly from a Computer-Aided Design (CAD) model using a layer-by-layer construction method [1,2]. Following ASTM standards, metal AM processes are categorized into two principal techniques, namely Powder Bed Fusion (PBF) and Directed Energy Deposition (DED). Although both methods follow a layer-wise approach, the mechanisms of these manufacturing processes are primarily distinct. In the DED process, the feedstock material is directly delivered into the melt pool generated by a laser or electron beam. Conversely, in the PBF processes, a heat source such as a laser or electron beam selectively melts the layer of powder already spread on the substrate [3,4].

The PBF technology is further classified into Laser Powder Bed Fusion (L-PBF) and Electron Beam Powder Bed Fusion (EB-PBF) methods, depending on the energy source used to melt the powder. The L-PBF process employs a laser energy source, whereas the EB-PBF process uses an electron beam source to produce parts. The L-PBF process, also known as Selective Laser Melting (SLM), Direct Metal Laser Melting (DMLM), or Direct Metal Laser Sintering (DMLS), enables the creation of custom-designed products with a higher level of accuracy and complexity than conventional manufacturing processes [5,6]. In these processes, a layer of powder is heated and melted following the CAD file and then solidified. Despite their differences, these processes share the same technological features, as depicted in Fig. 1. Specific points of the powder bed are selectively scanned along predefined paths with the laser source energy. The selectively melted powder layer cools down and solidifies, forming a new product layer. Upon finishing the first layer, the powder dispenser platform moves upward to supply the required material for creating a new layer. The building platform lowers a distance equal to the layer thickness, and the recoater transfers the material

* Corresponding author.
** Corresponding author.
E-mail addresses: mohammadhossein.mosallanejad@polito.it (M.H. Mosallanejad), abdollah.saboori@polito.it (A. Saboori).

https://doi.org/10.1016/j.jmrt.2023.11.049
Received 12 September 2023; Accepted 6 November 2023
Available online 11 November 2023

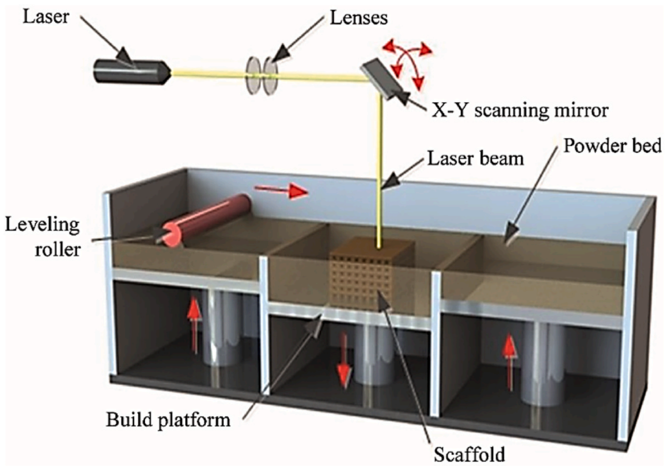

Fig. 1. L-PBF system schematic [9].

to the building platform, forming a new stratum. This same cycle repeats until the final shape is achieved [7,8].

One of the primary benefits of AM is its freedom of design in producing net-shape parts, particularly in high-performance applications. Recently, this technology has generated increased interest, particularly for its applications in the design field for automotive and aerospace industries, the manufacturing parts for energy industries (nuclear, oil, and gas), and the production of medical prostheses and implants, some of which are listed in Table 1 [10]. Nevertheless, the L-PBF suffers relatively low efficiency concerning traditional manufacturing techniques, leading to higher costs [11–14]. Furthermore, to produce components with enhanced accuracy and quality, the L-PBF machine is limited by a substantial production time, resulting in a drastic productivity reduction, as shown in Fig. 2.

L-PBF is primarily employed for high-end components with small production volumes where high costs are feasible [16]. As a result, several endeavors have been undertaken to address this issue and broaden the technology application [17–20]. For instance, some studies have focused on developing multi-laser systems that can simultaneously melt multiple regions of the powder bed, increasing the build rate [21–23]. Other researchers have investigated using preheated powders, allowing faster melting and solidification [24–26].

Additionally, implementing new scanning strategies, such as bidirectional scanning and checkerboard patterns, has shown promising results in reducing build time while maintaining part quality [27–29]. Furthermore, integrating Artificial Intelligence (AI) and Machine Learning (ML) algorithms can optimize the process parameters in real-time, leading to faster and more efficient production [30–33]. These efforts to improve productivity and expand the scope of L-PBF demonstrate the technology potential to revolutionize the manufacturing industry.

Improving parts productivity and quality is a crucial research objective in part production through the L-PBF technology. Several investigations have attempted to resolve these problems. For instance, Eschner et al. [36] examined process monitoring and control strategies, and Egan and Dowling [37] studied in-situ process monitoring and control. Zhu and Han [38] reviewed powder-based metal AM processes,

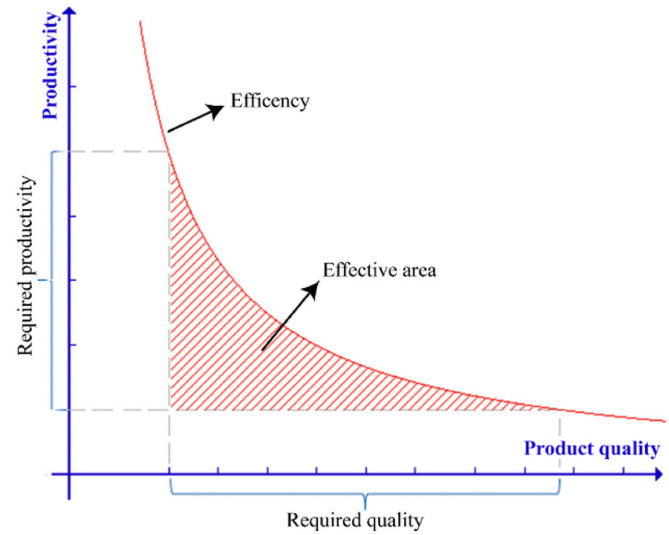

Fig. 2. Basic principles of L-PBF that are inversely related to its expansion and range of application compared with conventional metalworking processes [15].

materials, and properties comprehensively. Zhang et al. [39] explored process monitoring and control strategies to improve part quality. Other researchers examined the impact of laser power, scan speed, and hatch distance on L-PBF productivity and quality [40–43]. Despite all these efforts and to the best of the authors' knowledge, a comprehensive review paper on enhancing L-PBF productivity and part quality is not yet available in the literature. Hence, this study investigates the main process parameters and their effects on productivity and quality performances while providing appropriate productivity and cost equation models. Furthermore, principal approaches for selecting a process parameter combination that enhances build rate are explained using several case studies.

2. Process parameters

Processing conditions include machine settings (typically predefined) and process parameters that can be set depending on the case. In modern L-PBF systems, over 100 processing parameters can be classified into five categories, including laser-related parameters, scan-related, powder-related, atmosphere-related, and temperature-related (Fig. 3) [15,44,45]. Depending on the employed alloy and its final application, the parameters are optimized for full densification, high dimensional accuracy, low superficial roughness, and remarkable mechanical properties [46,47].

Amongst the factors, a few parameters, namely laser power, scan speed, hatch distance, layer thickness, and scanning strategy, considerably impact mechanical characteristics, economy, and ultimate quality of the entire L-PBF process [48,49]. The following sections briefly introduce these parameters, providing some collected quantities to analyze their combined effects. Besides these, their influence on the densification behavior and material properties are discussed further.

Table 1
Different alloys and their applications [34,35].

	Aerospace	Medical	Energy industries	Automotive	Marine	High-Temperature applications	Tools and molds
Aluminum	✓			✓			
Stainless steel	✓	✓	✓	✓	✓	✓	✓
Titanium	✓	✓		✓	✓	✓	
Inconel	✓				✓		

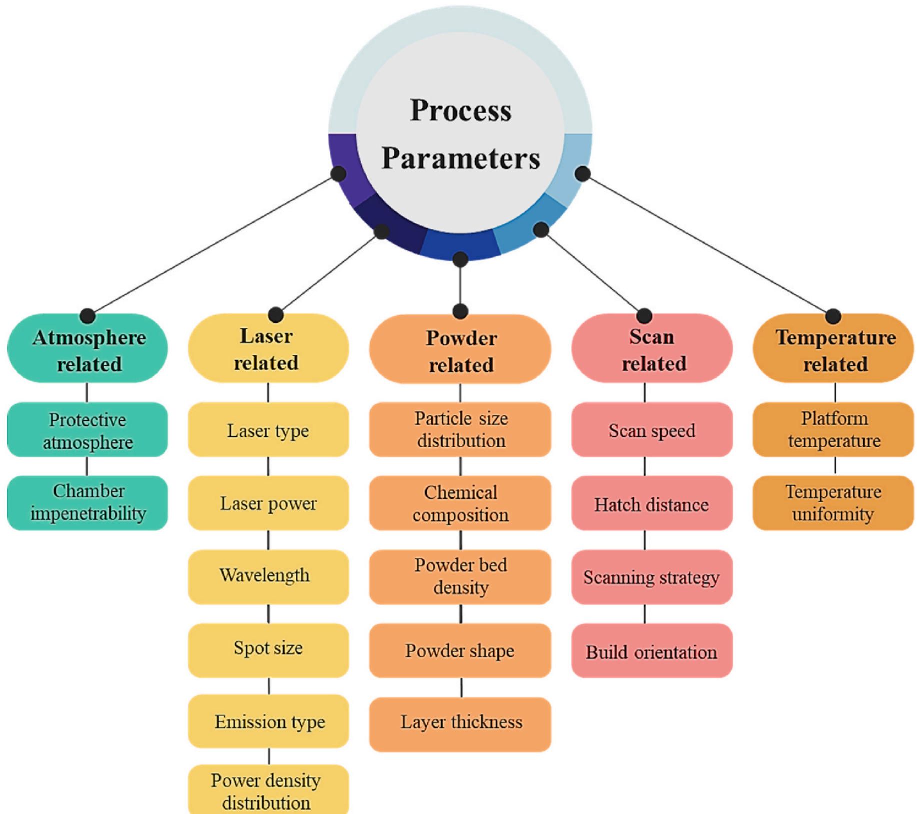

Fig. 3. Classified process parameters in modern L-PBF systems.

2.1. *Laser power (P)*

Laser power determines the magnitude of the temperature gradient on the powder bed, influencing the overall melting behavior and the material characteristics such as density, surface quality, morphology, and mechanical properties. The required laser power typically increases with the melting point of the material and lower platform temperature [44]. It is also varied depending on the layer thickness, scanning speed, and hatching distance to ensure the correct fusion of the processed material. Produced parts with lower porosity and higher density are commonly obtained when subjected to relatively high laser powers. Pragana et al. underlined that higher power values could lead to an acceptable density, allowing a flexible range for the other process parameters [50]. Leicht and Cacace also set the laser to the maximum allowable power of 200 W, adjusting the different variables to optimize several properties of the built part [10,51].

On the other hand, it is reported that despite the superior densification behavior, an extreme magnification of the laser power may result in the vaporization phenomenon and melt-pool instability with residual stresses and curling of the parts [44]. On the contrary, low laser power produces better dimensional accuracy, reducing densification and elevating vulnerability to layer delamination [44]. For these reasons, machine manufacturers offer their systems with laser powers ranging between 100 W and 400 W and, in the case of most modern solutions, up to 1 kW.

In a study by C. Keller et al., variations in laser power during a rescanning strategy were found to impact the microstructure and mechanical properties of Hastelloy X fabricated by powder bed fusion [52]. Decreasing the laser power by 40% during the second scan resulted in improved mechanical properties. Similarly, Montero-Sistiaga et al. observed that using a high-power laser in L-PBF of Hastelloy X increased production rates, coarser microstructures, and reduced hardness and yield strength [53]. Ho Yeung et al. proposed a laser power control algorithm based on the geometric conductance factor (GCF) to optimize powder bed fusion. Adjusting the laser power based on the proportion of solid or powder material near the melt pool improved melt pool intensity and part qualities such as surface finish and distortion [54].

Systems equipped with high-power lasers, most often with dual or quad laser solutions, exhibit a high gain in the productivity of the whole process. These machines offer several advantages, including the ability to process various materials and produce large components cost-effectively.

2.2. *Scan speed (v_s)*

Scanning speed is the forward velocity at which the laser beam moves over the powder bed. This parameter sets the amount of energy provided during the melting, contributing to the final surface quality of the part and the speed of the entire process.

According to the technical data sheets, L-PBF machines can reach very high speeds of 10,000 mm/s; however, in the literature examined, the values typically range between 220 and 3000 mm/s [16,50]. Indeed, high scan speed decreases the dwelling time and melt-pool temperature, leading to incomplete melting and dramatically increasing the part porosity, defects, and residual thermal stress [34]. However, an elevated velocity of the laser spot should be carefully associated with sufficiently high laser power and optimal hatch distance; otherwise, obtaining defect-free parts would be challenging [55].

Several studies have investigated the influence of scanning speed on microstructure, mechanical behavior, and surface quality. For example, Jiangwei Liu et al. examined the effect of scanning speed on 316L stainless steel fabricated through L-PBF and found that decreasing the scanning speed resulted in the formation of fine grains with high fractions of low-angle grain boundaries and fine cellular structures [56]. These microstructural changes led to improved ultimate tensile strength (UTS) and total elongation of the material.

Similarly, Mohd Faizal Sadali et al. focused on the influence of scanning speed on Ti6Al4V parts produced via L-PBF [57]. They determined that a scanning speed of 775 mm/s resulted in high-quality surface morphology and microstructure, exhibiting reduced splashing and balling effects. Furthermore, the maximum surface roughness values for both the upper and side surfaces fell within acceptable limits for biomedical applications [57]. These findings highlight the significance of scanning speed control in achieving desirable material properties and surface characteristics in L-PBF.

In addition to affecting microstructure and surface quality, scanning speed also impacts the dynamics of the molten pool during the L-PBF process. Weihao Yuan et al. conducted numerical simulations and experimental tests to investigate the temperature and velocity fields of the molten pool at different scanning speeds [58]. They identified three distinct states of the molten pool: unstable, transition, and stable states, each affecting surface defects and bulk density. Moreover, they observed that a slight depression region induced by the recoil pressure was beneficial for increasing the bulk density. At the same time, excessive energy input resulted in the formation of a keyhole and the production of residual pores. These findings demonstrate the intricate relationship between scanning speed, molten pool dynamics, and the resulting surface characteristics.

Generally, increasing scan speed to double directly improves productivity by decreasing the build time to half. Therefore, it is required to balance productivity and quality performance. Slightly lower-density products can be manufactured by increasing the build rate [59].

2.3. Hatch distance (h)

The spacing between two parallel laser tracks is typically called hatch distance. This parameter joins the spot size (*d*) and regulates powder melting, ensuring an adequate attachment between adjacent laser tracks. Neighbouring strips overlap to avoid pores between subsequent tracks or unfused powder zones. As can be seen in Fig. 4, an overlap in the tracks is necessary to obtain a dense solidification. In fact, by diminishing the hatch distance, the increase in the overlap of each laser pass becomes more evident, resulting in good surface roughness, low porosity, and high mechanical properties [60]. However, when the hatch distance reduces too much, the applied energy density rises, which can cause the overburning of the laser track outer edge and a warp and curve of the processed layer [55].

Furthermore, productivity dramatically decreases by increasing the number of scanned tracks. As reported in the literature, the typical range for the hatch distance is between 0.05 mm and 0.4 mm, depending on the other process parameters [50,61]. For these reasons, in most L-PBF processes, the hatch spacing is always lower than the diameter of the laser beam to ensure better quality [62]. The optimal hatch spacing can be calculated using Eq. (1):

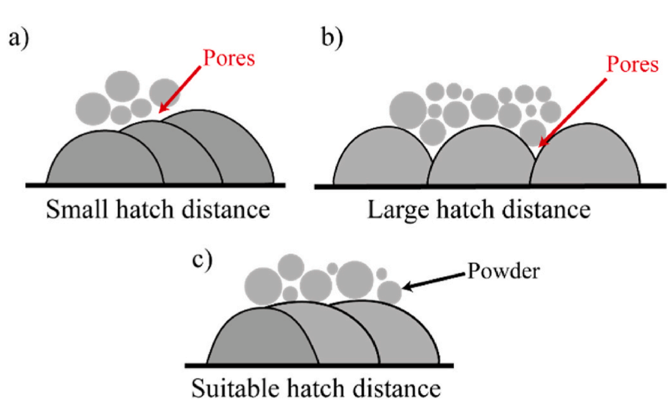

Fig. 4. Hatch distance and overlap [63].

$$h_{opt} = 0.25 \bullet d \tag{1}$$

In this equation, h_{opt} is the optimum hatch distance, and *d* is the laser spot size.

Extensive research has been conducted in recent years on the influence of hatch spacing on the productivity, quality, and cost of L-PBF parts. Dong et al. [64] investigated the effect of hatch spacing on 316L stainless steel (SS) samples fabricated by L-PBF. Their findings indicated that increasing hatch spacing resulted in a narrower melt pool width and deeper depth while coarsening the microstructures due to reduced cooling rates. An optimized hatch spacing of 100 μm was identified, producing fully dense parts with a smooth surface.

Saghaian et al. [65] focused on the L-PBF of NiTi alloys and explored the effects of hatch spacing and laser power. They discovered that decreasing hatch spacing improved the shape memory effect and increased the recoverable strain of the parts. The study also highlighted the influence of hatch spacing on surface morphology and identified an optimum hatch spacing of 120 μm for achieving the lowest surface roughness, making it suitable for bone implant applications.

Feng et al. [66] studied the L-PBF of NiTi alloy and investigated the effect of hatch spacing on pore defects, phase transformation, mechanical properties, and shape memory effect. The authors reported the evolution of pore defects from keyholes to gas pores and un-fused pores as the hatch spacing increased. The NiTi sample with a hatch spacing of 110 μm demonstrated superior tensile properties and shape recovery rate due to its low porosity and small-sized spherical gas pores. The study also identified residual internal stress, predominantly along the B2-(100) plane, and highlighted the contributions of different metallurgical factors to martensite transformation, with Ni evaporation identified as the major facilitating factor. Finally, these studies, along with other research in the field, highlight the significant impact of hatch spacing on the productivity, quality, and cost aspects of L-PBF parts.

2.4. Scanning strategy

The scanning strategy is the path the laser beam follows over the substrate [29]. Scanning often occurs in contour mode and hatch or fill mode. In contour mode, the beam scans the outer edge of a single layer. Scanning hatch and contour paths allows for better accuracy and surface finish. The most common hatch patterns are indicated in Fig. 5.

In fill mode, the laser scans the interior of the layer to build up the part. The most common fill trajectories are straight and parallel stripes, where each line is scanned sequentially, and the stripe angle is rotated after the scanning of every layer. Other fill strategies include concentric or meander routes and chessboard sections, each square being processed apart [44]. The choice of an appropriate laser pattern strongly influences the quality of the final component, particularly the magnitude of residual stresses. Many studies have shown residual stresses and subsequent part deflection increase with scan line extension. On the other hand, reducing the longest uninterrupted line of travel is beneficial for the final part features [9]. Based on these observations, dividing the scan area into squares of small segments and traversing two subsequent layers with different rotation angles successfully affects the residual stresses [59].

The elaborated trajectory of the laser spot guarantees an amplified accuracy. In contrast, optimized laser movements ensure minimum layer build time, which results in a great time saving for fabricating the whole part. Since the preferable strategy for improving the layer forming quality rarely corresponds to the fastest one, these two parameters should be adequately balanced [68]. The shape of the fabricated part also influences the choice of the scanning strategy. For example, contour scanning is preferred over hatch scanning for parts with sharp corners, while for parts with gentle slopes, hatch scanning is preferred for better surface finish and faster build time [69].

Different scanning strategies have been studied in the context of L-

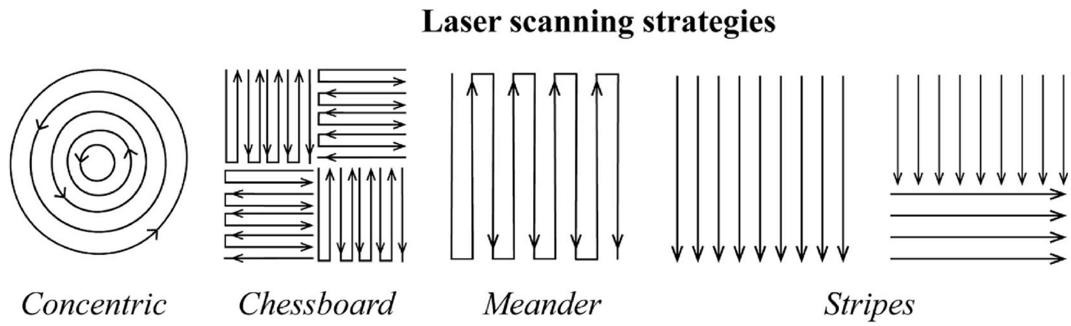

Fig. 5. Examples of scanning strategies used in L-PBF method [67].

PBF. For example, in the case of Stainless Steel 316L fabricated by L-PBF, rotation between layers disrupted columnar grain growth, resulting in fine equiaxed grains, improved tensile strength, and ductility [70]. Similarly, optimization of laser energy density and scanning strategy in 24CrNiMo low alloy steel led to higher specimen density, improved surface quality, and the desired lower bainite microstructure, enhancing strength [71]. In the case of 15-5 PH stainless steel, the island scanning strategy resulted in high-densification samples with fine grain structures, improving strength and elongation without needing precipitation hardening treatment [72]. In L-PBF of Inconel-718 alloy, larger island sizes contributed to higher relative density, but the 2×2 mm^2 island scanning strategy showed cracking and more pores. Mechanical properties were similar across all samples, with the 22-scanning strategy exhibiting the lowest residual stress [73].

2.5. Layer thickness (l)

The layer thickness refers to the height of a single slice generated from the CAD model, which is regulated by the downward movement of the machine build platform. This parameter typically ranges from 20 to 80 μm [16]. Choosing an appropriate layer thickness is critical to achieving a high-quality component in L-PBF. The lower layer thickness is suitable for high-resolution parts, resulting in improved dimensional accuracy and lower surface roughness of the finished piece [69]. On the contrary, in the case of higher thicknesses, the energy source may not be sufficient to guarantee the correct fusion and cohesion between two successive layers, leading to a decline in the density and mechanical properties of the fabricated component [74].

It is well documented that L-PBF efficiency increases with the slice thickness as a layered manufacturing method if the other parameters remain constant. A faster build speed can be achieved by decreasing the total number of layers and required build time. However, the achievable productivity is limited by the degradation of the tensile properties of the fabricated parts under higher layer thicknesses. Therefore, balancing the maximum permitted layer thickness and excellent tensile properties is one of the critical points of L-PBF optimization [60].

Shi et al. [75] examined the impact of high layer thickness on the surface quality and defect behavior of Ti–6Al–4V fabricated through the L-PBF. They observed that increasing the layer thickness resulted in a significant deterioration in surface roughness, while density and tensile properties were relatively unaffected. However, samples with a layer thickness of 100 μm exhibited optimal mechanical properties similar to those obtained using thinner layers. In contrast, samples fabricated with a layer thickness of 200 μm showed lower tensile properties due to defects and the formation of different microstructures.

In a different study, Cutolo et al. [76] explored the influence of layer thickness on the fatigue properties of CoCr scaffolds produced by L-PBF. They found that increasing the layer thickness from 30 μm to 60 μm significantly improved the production rate without compromising the final structure geometry. Fatigue testing showed no significant differences in fatigue performance among the samples with different layer thicknesses.

Furthermore, Leicht et al. [16] investigated the implications of increasing the layer thickness for stainless steel 316L parts fabricated through L-PBF in terms of productivity and quality. They observed that increasing the layer thickness from 20 μm to 80 μm allowed for 4X faster fabrication without compromising the tensile strength. However, the 80 μm layer thickness resulted in some lack of fusion defects and reduced elongation to fracture. Nevertheless, the mechanical properties of the parts with larger layer thicknesses still met the standard specifications for cold-rolled Stainless Steel 316L.

Formanoir et al. proposed a hull-core strategy to balance productivity requirements and part accuracy. As shown in Fig. 6, this strategy involves setting high productivity and accuracy parameters for the core and outer regions, respectively [5]. This approach ensures excellent surface finish and resolution for the outer surface and higher productivity for the inner areas of the part.

These studies collectively highlight the importance of layer thickness in L-PBF processes. While higher layer thicknesses can improve productivity, they may also negatively impact surface quality, defect behaviour, and mechanical properties. Understanding the trade-offs between layer thickness and these key parameters is crucial for optimizing fabrication and achieving desired part quality and productivity.

2.6. Combined process parameters

Process parameters, which are shown in Fig. 7, are strongly interdependent and mutually interacting in the L-PBF process [44]. It should be underlined that laser power (P), scan speed (v_s), hatch distance (h), and layer thickness (l) determine the input energy transferred to the area of the expanded melt pool [61].

It was found that the energy-input characteristics for L-PBF are essential in process optimization. A straightforward quantity is the Linear Energy Density (LED) defined by the following equation (Eq. (2)):

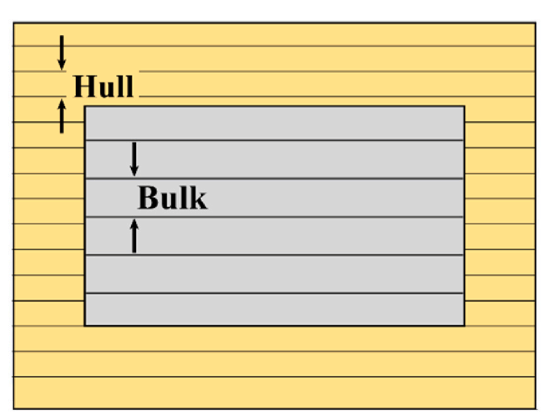

Fig. 6. Hull-Bulk strategy [5].

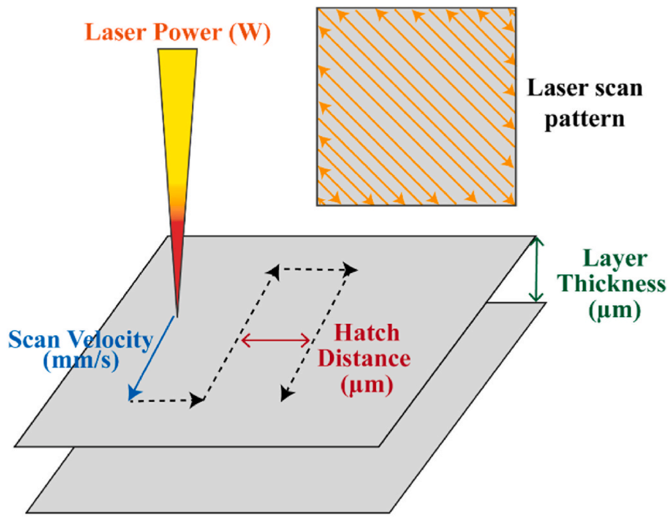

Fig. 7. Dominant process parameters in the L-PBF process [46].

$$LED = \frac{P}{v_s}\left[\frac{J}{mm}\right] \quad (2)$$

where P and v_s are laser power and scanning speed, respectively. Several authors have used this parameter to optimize geometrical accuracy and surface roughness [67]. However, applying process window diagrams makes mapping combinations of the involved parameters possible to obtain products with optimum density and reduced porosity [44].

Area Energy Density (AED) is the second quantity used to quantify the amount of provided energy by the laser (Eq. (3)).

$$AED = \frac{P}{h \bullet v_s}\left[\frac{J}{mm^2}\right] \quad (3)$$

P, v_s, and h are laser power, scanning speed, and hatch distance, respectively. AED is a physical quantity that specifies the amount of energy received by the cross-section of part during the laser fusion process. Moreover, numerous researchers have employed AED as a simple method for correlating input factors with the processing conditions for single-layer fabrication. Hence, it introduces an effective criterion for studying the formation of the inter-track pores [77]. The Volumetric Energy Density (VED) is the most comprehensive function, defined by Eq. (4).

$$VED = \frac{P}{l \bullet h \bullet v_s}\left[\frac{J}{mm^3}\right] \quad (4)$$

where l is the layer thickness, VED is the primarily adopted quantity to correlate process parameters with the mechanical, geometric, and density properties. From a physical point of view, it indicates the absorbed energy by a unit volume during the process, which can be used as an indicator to select the optimum range of parameters to cope with multiple objectives [67]. Moreover, the combination of process parameters and their optimization are crucial factors for the L-PBF process [44]. The optimal combination of parameters can enhance the quality and productivity of the fabricated parts, while improper settings can result in defects and low efficiency. In addition, the interaction between the parameters can affect the process performance and part properties [78].

Typically, the range of VED employed falls between 30 and 210 J/mm^3, depending on the chemical composition of the processed powder. In certain cases, self-built systems may utilize exceptionally high VED values. There are cases reported in the literature where the properties of samples, despite having identical VED values, displayed significant variations [79]. This observation aligns with the current uncertainty surrounding the role of energy density in the literature, which remains unresolved. Therefore, several researchers have investigated the effect of varying multiple process parameters on the quality of L-PBF parts, including the interactions between the parameters [80,81].

In addition to the above methods, the utilization of high-speed beam oscillation (Fig. 8) presents a compelling strategy for achieving a hierarchical distribution of laser energy in both spatial and temporal dimensions. This technique, first published by Wu et al. [82] during the L-PBF process, holds the potential to enhance productivity and, by manipulating the melt-pool shape, exert a more significant influence on the resulting microstructure of AM parts. Consequently, this can lead to improved quality of the manufactured components.

3. Productivity

Conventional manufacturing technologies often suffer from limitations in production rate, and L-PBF is not an exception, so the primary challenge with this method lies in its efficiency. The previous studies emphasize that enhancing the precision of the design and technological aspects of the part shape results in a significant increase in production time. However, extensive research is underway to develop methods for improving the efficiency of L-PBF [10]. The low production rate of the L-PBF process can lead to high production costs for each part, limiting the use of metal AM in various industrial fields. Factors contributing to high production costs include machines, raw materials, energy, gas, and build time [51].

Several cost models have been proposed for the AM processes. Alexander et al. [83] developed a standardized cost model considering specific characteristics of AM technology, such as part orientation and support structures. Hopkinson and Dickson [84] tailored a cost model for SLS, focusing on consistent processing times for identical elements. Ruffo et al. [85] expanded the SLS cost model to include direct and indirect costs, providing a comprehensive analysis. These models enhance cost estimation in AM by accounting for essential processes and various cost factors. Rickenbacher et al. [86] introduced a novel cost model designed explicitly for L-PBF. Unlike other models, this approach considers all process characteristics and adequately accounts for pre-and post-processing operations, making it more suitable for AM with L-PBF.

To quantify the productivity of the L-PBF technology, researchers used the part volume produced (V_p) per the total processing time (T_P) [15]:

$$PR = \frac{V_p}{T_P}\left[\frac{cm^3}{h}\right] \quad (5)$$

3.1. Processing time

Processing time is a critical factor that directly impacts the productivity of the L-PBF process. The total processing time is defined by Eq. (6), which consists of three main components [78]:

$$T_P = T_{pre} + T_{bld} + T_{post} \quad (6)$$

The pre-processing time (T_{pre}) includes activities such as machine setup and loading of the STL file. This is an essential step that directly impacts on the quality and accuracy of the final produced part. The build time (T_{bld}) accounts for the time needed to build parts. The build time can be affected by various parameters, such as the size and complexity of the component, laser power, laser scan speed, layer thickness, and hatch spacing.

The post-processing time (T_{post}) generally considers operations such as support removal and other treatments on the object. This step is crucial in removing any remaining powder and support structures while ensuring the final dimensional accuracy and surface quality of the components. Researchers have proposed several approaches to increase productivity and reduce processing time, such as optimizing process parameters, improving machine design, and developing advanced powder materials [85]. Herzog et al. [87] used a combination of L-PBF

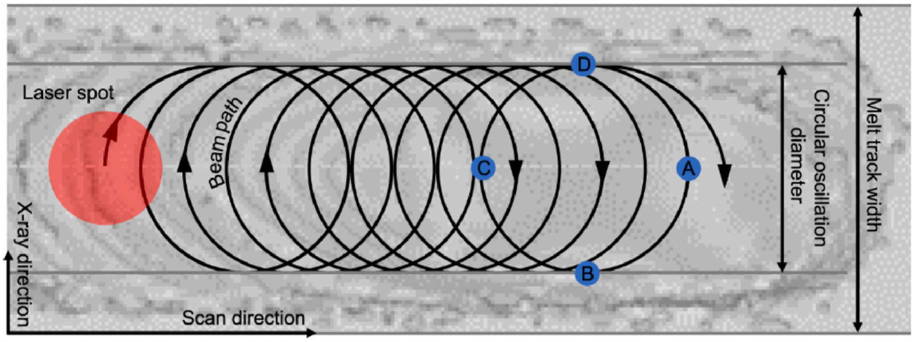

Fig. 8. A graphic illustration depicting the circular oscillation strategy used to enhance the productivity [82].

and subsequent HIP to enlarge the range of process parameters. This strategy aimed to approach higher reliability and quality or lower required laser power, reducing investment costs. Using HIP as a post-treatment would allow for employing higher scan speeds, lowering T_{bld}, and increasing the productivity of the L-PBF process.

Moreover, using multiple lasers and developing parallel processing methods have also shown promising results in reducing the build time and increasing the throughput of the L-PBF process [80,81].

3.2. Build time model (T_{bld})

The total processing time for AM includes the pre-processing, build, and post-processing times. Among these, the build time (T_{bld}) is a critical factor that affects the overall efficiency and productivity of the AM process. It can be further divided into three sub-components: delay time (T_d), recoating time (T_r), and material scanning time (T_s). As Eq. (7) shows, the build time is the sum of these sub-components [44].

$$T_{bld} = T_d + T_r + T_s \tag{7}$$

The delay time is the time required for the platform to lower to the correct position for the recoating system to deposit a new layer of powder. The recoating time is needed for the recoating system to spread the material on each layer for further processing. Finally, the material scanning time is the time required for the laser source to melt each layer.

Improving the efficiency of the build time is a crucial research direction for increasing the productivity of AM processes. Optimizing the build parameters, such as scanning speed, laser power, and layer thickness, can lead to faster scanning times and, therefore, a reduction in the overall build time. In addition, using more efficient recoating systems, such as multi-blade or multi-roller systems, can reduce the recoating time and further increase productivity.

3.3. Build rate (BR)

The L-PBF process cycle time can be divided into primary and auxiliary process time. The main process time consists of the time needed to melt each layer (scanning time), while other operations are part of the additional process time [10]. The build rate, which represents the volume of material the process can melt per time unit, is a crucial factor for measuring the productivity of the L-PBF process (Eq. (8)). Therefore, it can be concluded that increasing the build rate can improve productivity and reduce the cost per part.

$$BR = v_s \bullet h \bullet l \left[\frac{mm^3}{s}\right] \tag{8}$$

The most straightforward method to increase the building rate is to use a thicker powder layer with an enormous scanning speed and a more considerable hatch distance, as shown in Eq. (8). However, this approach can adversely affect the surface roughness, geometrical accuracy, and mechanical properties of the as-built components. Therefore, a trade-off between part quality and productivity is required to prevent defect formation and ensure the economic sustainability of the method. Various approaches have been implemented to address this issue, such as using machines with an enlarged build volume that can process multiple products simultaneously using twin or quad laser-scanning systems, different scan speeds, and build volume, as shown in Table 2.

3.4. Cost model

AM technologies, such as L-PBF, are typically used to produce small batches of complex components due to their long build times. L-PBF processes can achieve high levels of complexity, resulting in functional components that are lighter and require less feedstock material. This is particularly useful for medical and aerospace applications where part-customization is crucial. In contrast, traditional manufacturing methods are preferred for relatively simple designs due to their economic advantages [91].

The total cost of a job produced using AM technology can be divided into direct and indirect costs. Eq. (9) expresses the divided cost, where the direct costs depend on the amount of material used, and the indirect costs depend on the machine working time [92].

$$C_{job}\ [€] = C_{direct} + C_{indirect} \tag{9}$$

The simplest cost model includes only material costs, considered as direct costs. Indirect costs include amortization, electricity, and gas consumption, as shown in Eq. (10).

$$C_{job} = C_{material} + C_{operating} = m_{material} \cdot p_{powder} + \dot{C}_{operating} \cdot T_{bld} \tag{10}$$

Material cost ($C_{material}$) is defined by multiplying the part volume V_{part} (cm^3), the material density) $\rho_{material}$ (kg/cm^3), and the powder price P_{powder} (€/kg), as expressed in Eq. (11) [44]. Two coefficients, K_s and K_r, are included to consider support materials and powder recyclability, respectively.

$$C_{material} = k_s \cdot k_r \cdot V_{part} \cdot \rho_{material} \cdot p_{powder} \tag{11}$$

The hourly machine cost includes all the specific contributions that affect indirect costs, such as machine overhead, electricity consumption, and gas consumption. The AM labour cost C_l (€) is generally negligible, as the time required for workers to perform operations is minimal. Eq. (12) shows the calculation of the hourly machine cost.

$$\dot{C}_{operating}\left[\frac{€}{h}\right] = \frac{P}{h_y \cdot a_y} + p_{el} \cdot c_{el} + p_{gas} \cdot c_{gas} \tag{12}$$

where:

P: machine purchase price (€)
h_y: hours of production per year (h/y)
a_y: amortization time (y)
P_{el}: electricity price (€/KWh)
C_{el}: electricity consumption (€/KWh)

Table 2
Some L-PBF Machines are available on the market [88–90].

Company	Process	Machine	Laser type, power (W)	Build volume (mm)	Layer Thickness (μm)	Scan Speed (m/s)	Build Rate (cm^3/h)
EOS	DMLS	EOS M280	Yb-fiber laser, 200 or 400	250 × 250 × 325	20–80	up to 7.0	7.2–28.8
		EOS M290	Yb-fiber laser, 400	250 × 250 × 325	20–100	up to 7.0	7.2–28.8
		EOS M400	Yb-fiber laser, 1000	400 × 400 × 400	20–100	up to 7.0	7.2–36.0
Concept Laser (GE Additive)	DMLM	M2 Series 5	The dual-laser system, 2 × 400 or 2 × 1000	245 × 245 × 350	25–120	up to 4.5	2 - 35 or 2 - 93
SLM SOLUTIONS	L-PBF	SLM 125	IPG fiber laser, 400	125 × 125 × 125	20–75	up to 10	up to 25
		SLM 280 2.0	Single IPG fiber laser, 400 or 700 Twin, 2 × 400 or 2 × 700	280 × 280 × 3 65	20–90	up to 10 m/s	up to 113
		SLM 500	Twin (2 × 400 W or 2 × 700) IPG fiber laser Quad (4 × 400 or 4 × 700) IPG fiber laser	500 × 280 × 365	20–90	up to 10	up to 171
		SLM 800	Quad (4 × 700) IPG fiber laser	500 × 280 × 850	20–90	up to 10	171

P_{gas}: gas price (€/l)
C_{gas}: gas consumption (l/h).

Table 3 presents the operating costs of machines computed with Eq. (12). The hourly rate is calculated based on the assumption that production is limited to 5000 h per year [93]. Since technology and new machine models are constantly being developed, the amortization time is five years. Electricity and gas consumption data have been taken from technical datasheets, with the electricity cost considered at 0.217 (€/KWh) and the gas price at 3.23 (€/m^3), assuming the machine building chamber is filled with nitrogen [94].

The working time of a machine is considered in the build time (T_{bld}), as shown in Eqs. (13) and (14). The delay time is assumed to be negligible compared to the total scan and recoating times. For instance, a single cycle (Trc) recoating time is approximately 8 s for the Concept Laser Mlab R machine. This simplified model does not consider the costs of material, machine preparation, and post-processing, which generally cannot be ignored. According to a survey, these costs account for 19% of the total production cost [95].

$$T_{bld}(s) = \frac{V_{part}[mm^3]}{BR\left[\frac{mm^3}{s}\right]} + \frac{Part\ height\ (mm)}{layer\ thickness\ (mm)} \cdot T_{rc}(s) \tag{13}$$

$$T_{bld}(h) = \frac{\frac{V_{part}(mm^3)}{BR\left(\frac{mm^3}{s}\right)} + \frac{Part\ height(mm)}{layer\ thickness\ (mm)} \cdot T_{rc}(s)}{3600} \tag{14}$$

Some cost models also consider the energy usage of the manufacturing step as a direct cost when assessing the life cycle of AM metal parts. In this case, energy usage is evaluated as the energy consumed to fabricate a unit mass of material (MJ/kg), often referred to as specific energy consumption (SEC). For L-PBF techniques, SEC varies between 80 and 600 (MJ/kg) [96], while Kellens et al. define it as 96.82 (MJ/kg) [97].

Table 3
The machine operating cost is calculated based on Eq. (12).

	Concept Laser Mlab R	EOS M290	SLM 500
Price (£)	131.150.00	574.000,00	1.230.000.00
Electricity consumption (KWh)	1.5	2.4	10
Gas consumption (m^3/h)	0.048	0.150	0.96
Operating cost (£/h)	5.73	23.97	54.47

4. Quality parameters

The quality of a final part is evaluated based on various parameters such as surface roughness, microstructure, porosity, and mechanical properties. Fig. 9 demonstrates how these parameters are considered. The optimized process parameters are determined based on one or more objectives, such as producing fully dense components, minimizing defects, reducing surface roughness, achieving desired mechanical properties, and increasing the build rate [46]. However, optimizing for quality and productivity is challenging, as these parameters often conflict.

This section analyzes the quality of as-built parts produced using the L-PBF process. It will take advantage of previous research on stainless steels, aluminum, Inconel, and titanium alloys to better portray the effects of laser power, scan speed, layer thickness, and hatch distance on the quality of final parts.

4.1. Surface roughness

Surface roughness is a crucial quality parameter in the L-PBF process. Various process parameters such as laser power, hatch spacing, layer thickness, and scan speed significantly influence the surface roughness of the final part. Reducing the hatch spacing to a certain optimal level generally reduces surface roughness in AlSI 316L and Inconel alloys [59, 98]. However, further reduction in the hatch spacing can lead to some drawbacks. Low laser power can also result in high surface roughness and low dimensional accuracy due to the incomplete melting of the powder layer by the heat source, especially with thicker layers. Increasing the laser power can reduce the roughness and improve the geometrical accuracy of the part. Nevertheless, this trend becomes unstable at high power and speed [98].

The scan speed also plays a significant role in the surface roughness of the as-built parts. A very high scan speed can cause incomplete melting of the powder bed surface, adversely affecting the surface quality, as shown in Fig. 10 [98]. Badrossamay et al. found no apparent trend between roughness and scan speed. However, a drastic increase in scan speed significantly reduced the surface roughness of built AlSI 316L samples [59]. Guo et al. observed that both too high and too low scan speeds could reduce the surface quality of Inconel specimens. Moreover, roughness parameters are slightly higher with greater layer thickness due to the larger melt pool formed with a thicker layer thickness [98]. All in all, it can be concluded that optimizing the process parameters is crucial to achieving a desirable surface roughness in as-built L-PBF parts.

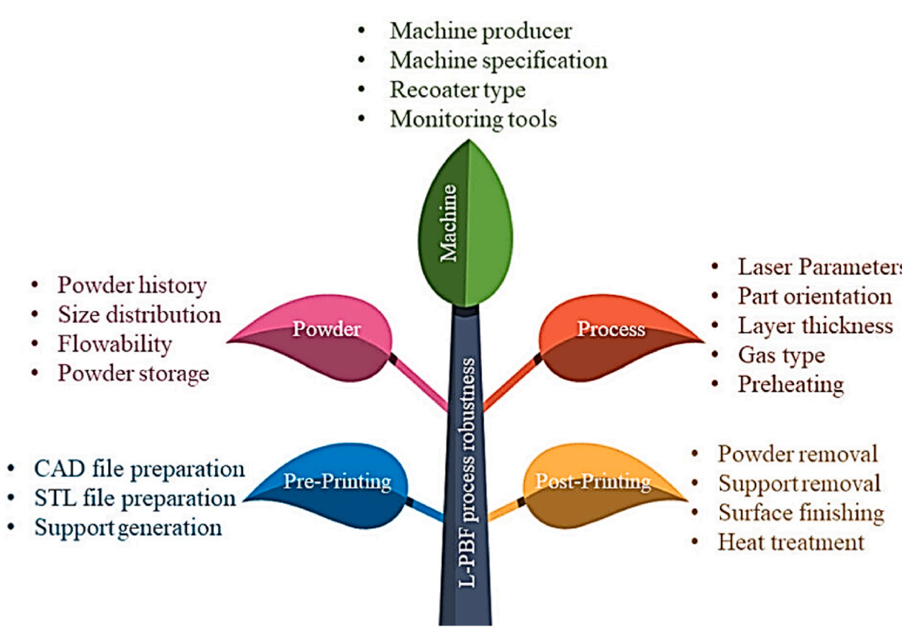

Fig. 9. Product quality parameters.

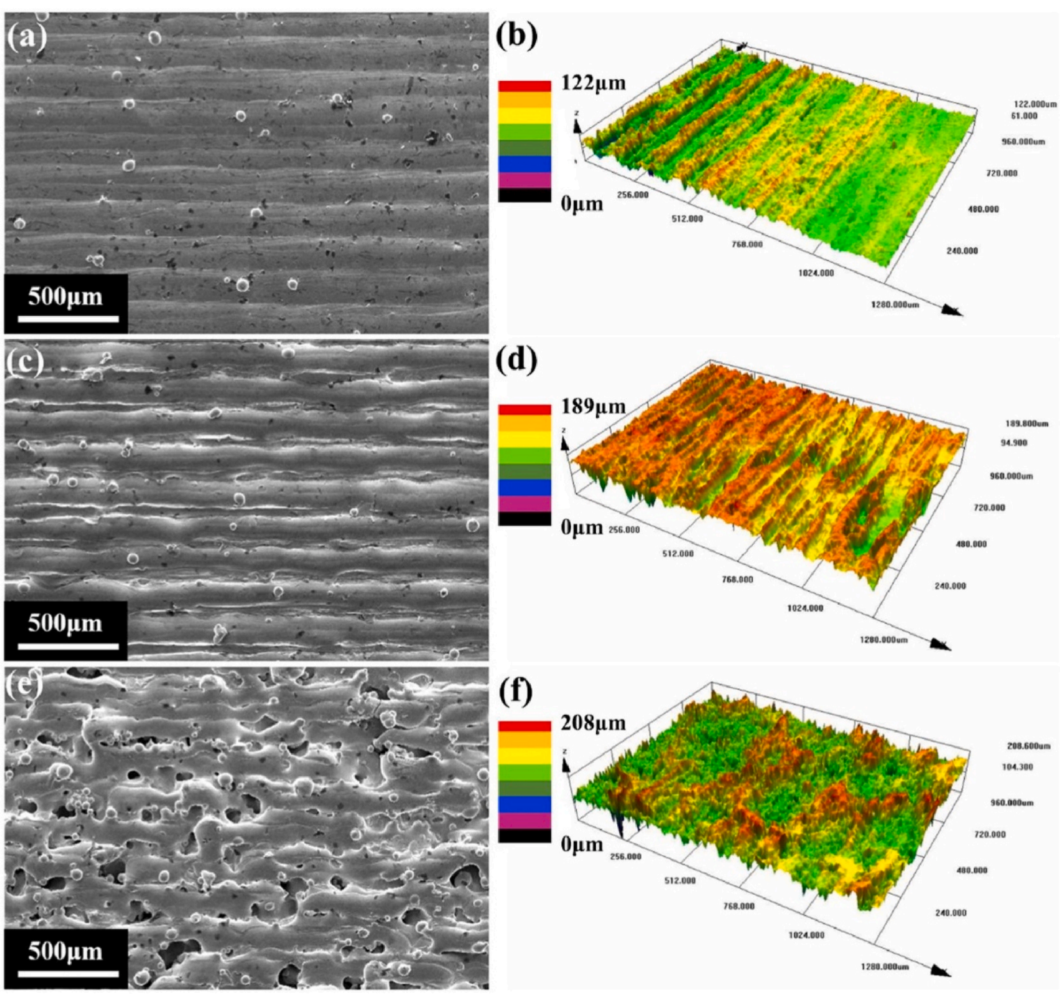

Fig. 10. Top surface SEM and reconstruction images at (a) 150 W, (b) 250 W, and (e, f) 350 W laser power (scan speed 2000 mm/s, hatch spacing 90 μm) [98].

4.2. Microstructure

The microstructure of components produced by the L-PBF process is complex, with elongated grains that can span multiple melt pool boundaries [51,99]. This microstructure is highly dependent on the processing parameters, which can be optimized to reduce defects, such as pores and cracks, and to produce a finer microstructure with superior mechanical properties [100,101].

Microsegregation, undesired texture, coarse columnar grains, and meta-stable phases such as martensite are common defects encountered in the microstructure of L-PBF-produced parts. Oliveira et al. [46] have reported that microsegregation can be eliminated by increasing or strongly reducing the laser velocity. At the same time, undesired texture and coarse/columnar grains can be mitigated by lowering the laser speed or reducing laser power. Remelting under reduced laser power is also recommended for eliminating meta-stable phases. It is crucial to minimize the occurrence of these defects to achieve a finer microstructure with superior mechanical properties.

4.2.1. AlSI 316L microstructure

L-PBF fabricated AISI 316L components typically exhibit a microstructure characterized by two main phases: face-centered cubic (FCC) austenite (γ phase) and body-centered cubic (BCC) ferrite (δ phase), which should not exhibit a martensitic phase under no strain [102,103]. Leicht et al. investigated the microstructural features of 316L-built samples and reported melting pool boundaries (MPB), high-angle grain boundaries (HAGB), and hexagonal cell boundaries shown in Fig. 11. Furthermore, the authors observed the presence of cell boundaries and nano-sized oxide particles, which may contribute to the material strength as their Si and Cr concentrations increased [51].

Eliasu et al. [104] investigated the microstructure of L-PBF-fabricated AISI 316L samples and reported two distinct microstructural features: cellular and columnar (or lathe) structures. They observed that increasing laser power led to more distinct substructures, with the boundaries of the cellular and columnar structures becoming thicker and better defined. This effect was also observed when modifying the scanning speed. Furthermore, increasing the hatch spacing resulted in the boundaries of the cellular and columnar structures becoming less distinct and thinner, with a relatively sparse distribution of the columnar structures.

Conversely, decreasing the hatch spacing led to densely packed cellular structures with a relatively light distribution of the columnar structures [104]. Leicht et al. [16] also investigated the microstructure and mechanical properties of AlSI 316L samples with 20 μm and 80 μm layer thicknesses, respectively. They adjusted the process parameters, including $P = 220$–370 W, $v_s = 800$–2100 mm/s, $h = 0.09$–0.12 mm, and with a VED ranging from 19 J/mm^3 to 77 J/mm^3. They evaluated the build speed and the process stability to determine the process window. The process stability was assessed using the standard deviation of the grey values in the EOS M290 system linked to the melt pool intensities. A high standard deviation indicated widespread intensities and a less stable process. The grey values standard deviation was found to rise globally by increasing VED. The process was unstable for a VED greater than 50 J/mm^3. The results, which are shown in Fig. 12, suggested that parts can be fabricated four times faster with tensile strengths comparable to those obtained using standard process parameters. Both layer thicknesses achieved a density greater than 99.9%, but a lack of fusion defects in samples produced with an 80 μm layer thickness was found.

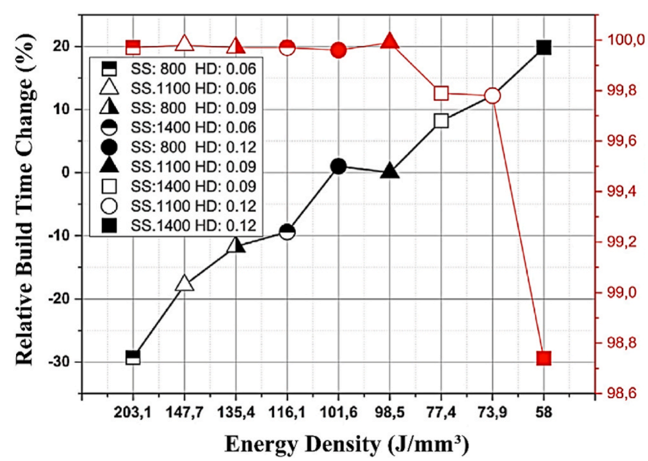

Fig. 12. Graph of relative build time and density as a function of VED [16].

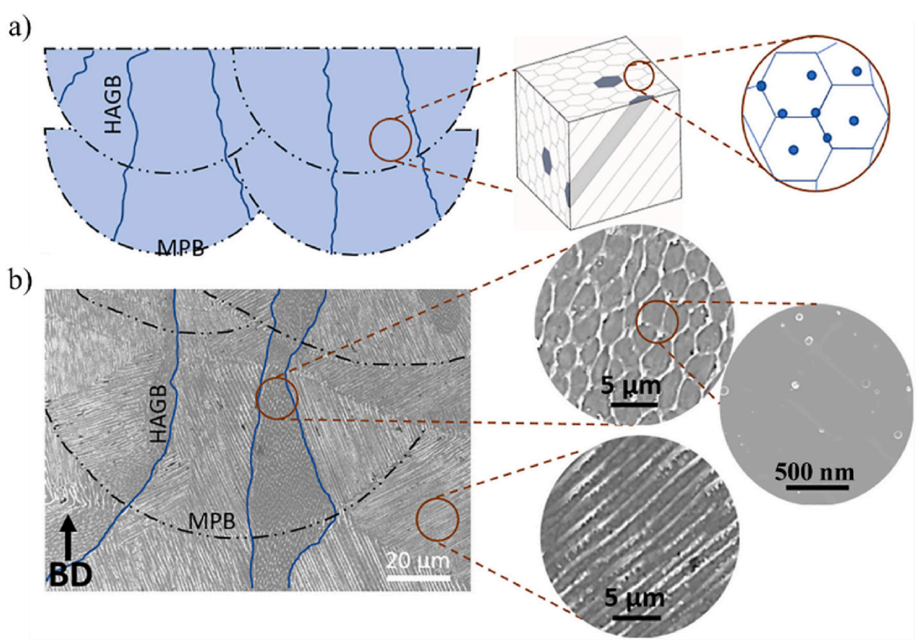

Fig. 11. L-PBF 316L microstructure general features [51].

4.3. Porosity

Porosity is a well-known issue in metal parts that can harm mechanical properties. Process-induced porosity occurs during manufacturing and can be classified into two main types: lack of fusion and keyhole porosity. Lack of fusion porosity happens when the energy applied is insufficient to cause complete melting. Factors such as scan strategy, power, scan velocity, hatch distance, and layer thickness play a role in this porosity type [46]. The pores created by a lack of fusion porosity are usually thin, non-spherical, and crescent-shaped [105].

On the other hand, keyhole porosity is formed due to irregular melt pool dynamics, where gas is trapped within the solidified material. This porosity is often caused by excessive laser power, which vaporizes the metal and results in increased recoil pressure and spatter ejection. The main contributors to keyhole porosity are laser power and scan velocity. While changes in layer thickness and hatch distances have little effect on this type of porosity, scan strategy can play a role. Laser power can be reduced, or scanning speed can be increased to prevent keyhole porosity [46].

Porosity is also influenced by the VED, which can strongly impact the total porosity. Low VED values lead to increased porosity because of the grown unfused powder within the layers. Increasing VED, however, can help to improve melting and the flow of molten material, thereby reducing the pores. However, when the energy density is too high, porosity can increase again due to the keyhole effect. Studies, such as the one by Eliasu et al. [104], have found a clear relationship between porosity and VED while examining the microstructure of built AISI 316L parts. Other researches has shown that this evolution is typical for other metallic alloys, too [10].

4.4. Densification behavior

Successfully producing high-quality L-PBF components requires carefully selecting optimal processing parameters to achieve a density above 99% [106]. However, specific process parameters such as increasing hatch distance and vector scan size can have a negative effect on density [50]. On the other hand, increasing laser power has a positive effect on density, while excessively high or low scan speeds, particularly when paired with high hatch spacings, can lead to decreased density. Combining various process parameters can identify a steady region where optimal processing conditions can be utilized to achieve good mechanical properties (Fig. 13). Researchers have reported different VED values that ensure desirable densifications (Table 4).

4.5. Mechanical properties

Analysis of the mechanical properties of L-PBF-designed components shows that it is possible to produce high-strength alloys, even exceeding the performance of parts produced by conventional manufacturing methods. The mechanical performance of L-PBF alloys is mainly due to the fine microstructure and the supersaturated solid solution obtained by the rapid solidification effect. Table 5 summarizes the mechanical properties of L-PBF-produced parts.

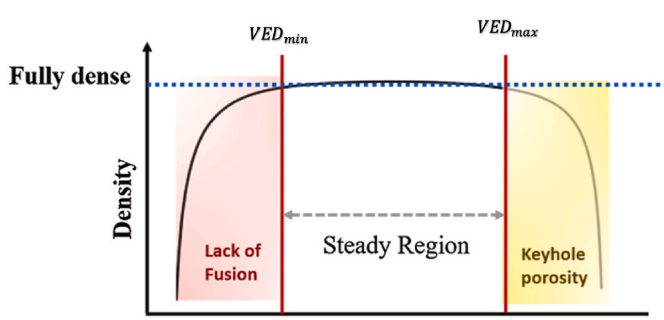

Fig. 13. Density as a function of VED [10].

Table 4
VED ranges for optimal densification.

Machine	Material	Optimal VED for dense parts (J/mm^3)	Ref
EOS M280	316L	40–100	[104]
EOS M280	316L	62.5–104.2	[107]
AM250 Renishaw	316L	104.52	[108]
EOS M290	316L	37–65	[16]
EOS M290	316L	73.9–203.1	[51]
AM250 Renishaw	A357	85–140	[10]
Concept Laser M2	AlSi10Mg	60–75	[109]
EOS M270	IN625	78–110	[110]
Concept Laser M2	IN738LC	55–75	[98]
DiMetal-280	Ti6Al4V	250	[111]
ProX DMP 320	Ti6Al4V	30.2–58.9	[5]

Table 5
Mechanical properties and surface roughness characterization of L-PBF-manufactured components.

Machine	Material	Property	Ref
EOS M280	316L	Hardness: 208.7–241 HV	[104]
AM250		Hardness: 225 HV Surface roughness: 9–16 μm	[108]
EOS M290		YS: 460–540 MPa UTS: 600 MPa E: 44–61%	[16]
EOS M290		YS: 452–483 MPa UTS: 525–575 MPa E: 33–52%	[51]
–		YS: 521 ± 101 Mpa UTS: 610 ± 80 MPa E: 32 ± 17% YM: 180 ± 25 GPa	[112]
HRPM-II SLM		Microhardness: 255 HV UTS: 321–722 MPa	[113]
ProX DMP 320		UTS: up to 707 MPa E: 30–55%	[56]
AM250	A357	YS: 202.5–217.6 MPa UTS: 393 ± 7.4 MPa E: 10.5 ± 1.6%	[10]
Concept Laser M2	AlSi10Mg	YS: 240–275 MPa UTS: 280–375 MPa E: 0.5–2.25%	[109]
EOS M270	IN625	Hardness: 31.8–69.3 HRC	[110]
Concept Laser M2	IN738LC	Surface Roughness: 11.16–21.1 μm UTS: 300–1200 MPa E: 3.5–11%	[98]
DiMetal-280	Ti6Al4V	Hardness: 492 HV	[111]
ProX DMP 320		Top Roughness: 4.16 ± 0.5 μm Side Roughness: 6.95 ± 0.2 μm YM: 68–113 GPa YS: 1016–1111 MPa E: 7.8–10.3%	[5]

UTS: Ultimate Tensile Strength; YS: Yield Stress; E: Elongation; YM: Young's Modulus.

Mechanical results of the produced components showed that the properties of manufactured parts strongly depend on the building parameters used during the process, as exhibited in Table 6 [62]. Density is a crucial factor directly affecting the mechanical properties of the products. Favorable mechanical properties can be achieved by reducing the porosity to <1% [114]. Guo et al. [98] found that too high or too low υ_s increased the porosity of IN738LC-built samples.

Tensile strength, Young's modulus, microstructure, elongation at the break, tensile yield strength, and ultimate tensile strength depend on the layer thickness [48]. These properties tend to decrease concerning the increase of layer thickness. The main reasons for higher hardness and tensile properties are finer grain size, cellular microstructure, and well-distributed nano-sized precipitates [115]. Despite this, Shi et al. outlined that high layer thickness influences surface roughness rather than tensile properties during the L-PBF process [116]. Besides, an

Table 6
Effects of processing parameters on the final quality of the product.

Machine	Material	Processing parameters	Effect						Ref
			Porosity	Surface roughness	Hardness	Density	Elongation	Tension strength	
EOS M280	316L	hatch spacing and laser scan speed ↑	↑	–	–	–	–	–	[104]
		laser power ↑	↓	–	–	–	–	–	
Concept Laser M2	AlSi10Mg	laser scan speed ↑	↑	–	–	–	–	–	[109]
EOS M270	IN625	hatch spacing and laser scan speed ↑	–	–	↓	–	–	–	[110]
		laser power ↑	–	–	↑	–	–	–	
Concept Laser M2	IN738LC	hatch spacing and laser scan speed ↑	↑	↑	–	–	–	–	[98]
		laser power ↑	↓	↓	–	–	–	–	
EOS M280	316L		–	–	–	↑↓	–	–	[107]
HRPM-II SLM	316L		–	–	–	–	↑	↑	[113]
EOS M290	316L	layer thickness ↑	–	↑	–	–	↓	↓	[16]
DiMetal-280	Ti6Al4V		–	–	–	↓	–	–	[111]
Concept Laser M3	316L		–	↑	–	–	–	–	[59]

increment in the laser power increases the microhardness and tensile properties of products [74].

4.5.1. *Residual stress*

Residual stress is a significant concern in AM processes, such as L-PBF, as it can cause deformation, cracking, and delamination in as-built components [117]. The residual stress distribution in part typically exhibits two zones of significant tensile stresses at the top and bottom of the part and a large zone of intermediate compressive stress in the middle [118]. The magnitude of residual stresses can reach values above 500 MPa [102], often higher than the yield stress of the alloy. It is, therefore, crucial to control residual stresses to ensure the desired mechanical properties of the component.

Several methods have been proposed to mitigate residual stresses in L-PBF, including reducing the scan vector size, preheating the substrate, and using sacrificial supports to restrain part deformation [46]. These methods can help balance the residual stress distribution and prevent failure of the part. However, the effectiveness of these methods depends on several factors, such as material properties, process parameters, and part geometry. Therefore, it is essential to carefully evaluate the residual stress profile and choose the appropriate method to control it in each case.

5. Process optimization methods

This section will discuss practical optimization methods for the L-PBF process to achieve high productivity and high-quality products. Optimizing involves selecting the most suitable process parameters to achieve the desired quality and productivity. One standard method is the Design of Experiments (DOE), which involves systematically varying the process parameters to determine their effects on the part quality and productivity. Response Surface Methodology (RSM) is another method that uses mathematical models to predict the optimal process parameters for achieving the desired quality and productivity. Process mapping visualizes the process parameter space to identify optimal parameters for producing high-quality parts while minimizing production time. AI and ML algorithms can also optimize the process by learning from previous production data and predicting new process parameter combinations. Combining these methods can provide a comprehensive approach to optimizing the L-PBF process for high-quality and high-productivity production.

5.1. *Layer thickness optimization*

Increasing the powder layer thickness is the most effective way to improve productivity. It not only allows raising the build rate by reducing the building time but also decreases the overall production time by lessening the recoater run. Badrossamay et al. [59] reported that it is possible to obtain an improvement of 20–25% in productivity only by applying a thicker layer within a specific threshold limit. In addition, further enhancement could be achieved by processing at higher scanning speeds than the default values. However, attainable densities decreased since obtaining the same adequate melt pool would not be possible. Despite the significant enhancement in productivity, several defects in the sample with high thickness appear in the products due to a lack of fusion related to a lack of melting between layers. Moreover, the presence of such defects introduces stress concentration sites, which can be detrimental in the case of dynamic loading [16].

5.2. *VED method*

The VED method is highly effective in improving build speed, as reported by numerous researchers [10,51]. This method determines the minimum applied energy required for a sample to achieve adequate material fusion for the desired properties. Once selected, the fastest combination of laser power, scan speed, and hatch distance can be used to maximize productivity for a particular machine layout [44]. The work by Eliasu et al. [104] on AlSI 316L samples (Fig. 14) demonstrated the trend of VED versus porosity/density. By combining Eq. (4) and Eq. (7), it is possible to obtain the following relation:

$$VED = \frac{P}{BR} \tag{15}$$

The maximum *BR* corresponds to the VED minimum for a given laser power. This procedure allows for identifying a combination of parameters, ensuring increased productivity while maintaining a desirable density and pore content [10].

5.3. *Taguchi and ANOVA analysis*

The Taguchi Response Surface Method is a statistical approach widely used to optimize the parameters of powder bed fusion processes. The method involves selecting appropriate process parameters and good-quality characteristics based on experimental analysis and selecting the proper orthogonal array to conduct experiments. The experimental results are then analyzed using the signal-to-noise (S/N) ratio and statistical analysis of variance (ANOVA) to determine the optimal process parameters for improved productivity.

Dzukey et al. [119] applied the Taguchi Response Surface Method to evaluate the L-PBF process parameters, including laser power, scan speed, hatch spacing, and layer thickness, on the density of AISI 316L samples. The study showed that the optimized process parameters significantly improved the density of the samples, indicating the effectiveness of the Taguchi Response Surface Method in optimizing powder bed fusion processes.

Similarly, Calignano et al. [62] used the Taguchi and ANOVA techniques to optimize the DMLS process of aluminum parts by studying the impact of process parameters, including laser power, scan speed, and

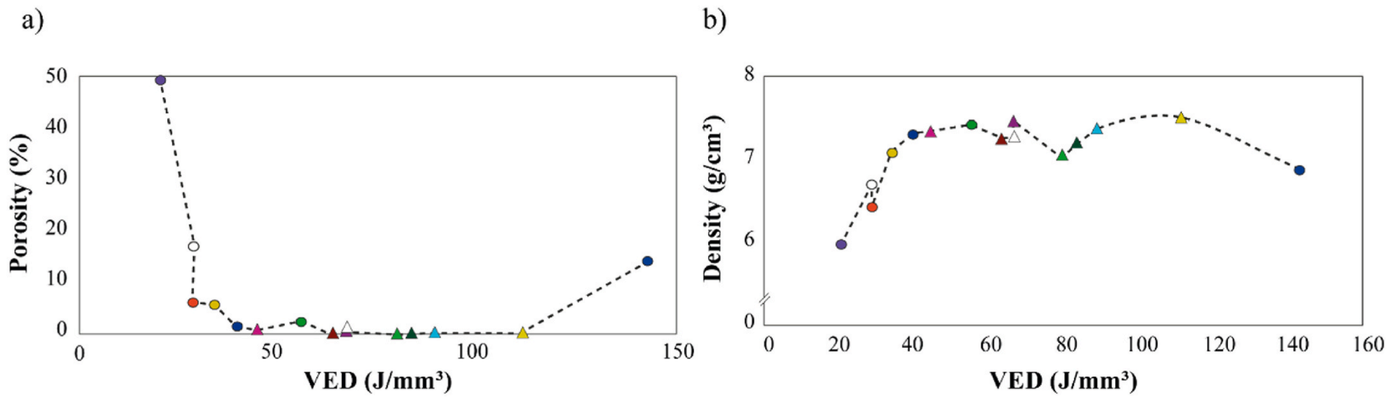

Fig. 14. Porosity and density versus VED experimental result [104].

hatch spacing, on surface roughness. The results showed that the optimized process parameters significantly improved surface roughness, demonstrating the usefulness of the Taguchi Response Surface Method in optimizing different aspects of powder bed fusion processes.

Therefore, the Taguchi Response Surface Method has been proven to be a practical approach to optimizing the parameters of powder bed fusion processes, leading to improved productivity, quality, and efficiency.

5.4. Optimization algorithms and numerical modeling

Artificial Neural Networks (ANN) and numerical modeling are advanced techniques that have shown promise in optimizing the L-PBF process while achieving the desired part quality. Marrey utilized an ANN algorithm to establish the relationship between process parameters and part quality, which was then used to optimize process parameters to achieve the desired properties [48]. This study provides a framework for mapping the final quality of a fabricated part to the process parameters. This correlation enables the development of an intelligent neural network that suggests process parameters and estimates build-time.

On the other hand, Letenneur proposed a simplified analytical model for the melt pool of the L-PBF process [120]. This technique contributed to developing a density prediction approach tailored to powder feedstock and L-PBF systems. The numerical modeling consisted of a thermal field model created by a moving heat source on a solid body to determine the melt dimensions for the selected printing parameters. This method reliably optimized the laser powder bed metal fusion process. It was validated for different alloys and processing conditions using literature data, demonstrating its potential for L-PBF process optimization. ANN and numerical modeling are sophisticated techniques that can enhance the L-PBF process. These approaches help identify the optimal process parameters and predict the final product desired properties.

In conclusion, each optimization technique discussed in this section presents its own set of advantages and limitations, making them suitable for specific L-PBF methods. Among these techniques, layer thickness optimization is a relatively straightforward and effective method that can significantly enhance productivity by reducing build time. However, to prevent the occurrence of defects and stress concentration in the final product, it is imperative to carefully consider the threshold limits. The VED method, on the other hand, identifies the minimum energy required for material fusion to increase build speed. It offers a methodical approach for selecting laser power, scan speed, and hatch distance configurations to maximize productivity.

The Taguchi method, used in conjunction with ANOVA, provides a statistically accurate means of optimizing the L-PBF process. This practical strategy is effective in identifying optimal parameters based on experimental results. However, its efficacy is heavily reliant on the selection of appropriate process parameters and quality characteristics for analysis. The use of suboptimal parameters may impede the achievement of intended enhancements. To overcome this limitation, advanced techniques such as artificial neural networks (ANN) and numerical modeling can be utilized to optimize the L-PBF process and predict the desired part properties. The effectiveness of models depends on the quality of data and their precision, which may require specialized software and knowledge for complex numerical modelling.

6. Conclusions

AM processes have revolutionized the manufacturing industry by offering the ability to produce complex parts with high quality and minimal material waste. L-PBF, an AM variant, has emerged as a popular choice for processing metallic alloys with good quality and enhanced productivity. While L-PBF can produce parts with optimal quality and mechanical properties, achieving this goal has been a significant challenge. By adopting L-PBF with optimized productivity, substantial cost savings and efficiency enhancements can be achieved in various applications ranging from biomedical devices to automotive production. Hence, this review paper offers an overview of the latest advancements in productivity, quality, and cost perspectives of the L-PBF processes. The following concluding remarks can be drawn from the current text:

- Optimizing the production cycle is crucial for successful completion of the manufacturing process, as increased cycle times can result in higher costs and limited mass production. Several strategies have been studied to investigate the low productivity issue of the L-PBF process, from modifying the hardware to optimizing the process parameters.
- The assessment of L-PBF products involves the examination of critical quality factors, including surface roughness, microstructure, densification behavior, component porosity, mechanical properties, and residual stress. These factors play a significant role in determining the outcome of L-PBF products and are essential for ensuring the reliability, functionality, and safety of the end products. Thus, a comprehensive understanding of these quality factors is crucial for optimizing the L-PBF process and producing high-quality products that meet the desired specifications and requirements.
- The implementation of optimization strategies becomes crucial in order to tackle these concerns effectively. The examined methodologies encompass strategies such as augmenting layer thickness, employing the VED method, utilizing the Taguchi statistical approach, and employing optimization algorithms and numerical modeling to improve both productivity and quality. These methods can increase productivity compared to the standard values while guaranteeing favorable quality properties.
- These approaches also demonstrate a correlation between the process parameters and production time, resulting in several parameter

sets that can accelerate production without compromising mechanical properties. Even with these approaches, build rates remain low, and further studies are needed to optimize set parameters and develop new technologies. Innovative hi-tech machinery is required to enhance current values and improve the technology.

In conclusion, L-PBF offers a promising future for the manufacturing industry, and continued research and development will help to unlock its full potential. By leveraging the various approaches discussed in this review and exploring new strategies, the industry can overcome existing challenges and reap the many benefits of L-PBF.

Declaration of competing interest

The authors declare that they have no known competing financial interests or personal relationships that could have appeared to influence the work reported in this paper.

References

[1] Matilainen V, Piili H, Salminen A, Syvänen T, Nyrhilä O. Characterization of process efficiency improvement in laser additive manufacturing. Phys Procedia 2014;56:317–26. https://doi.org/10.1016/j.phpro.2014.08.177.

[2] Aversa A, Saboori A, Marchese G, Iuliano L, Lombardi M, Fino P. Recent progress in beam-based metal additive manufacturing from a materials perspective: a review of patents. J Mater Eng Perform 2021;30:8689–99. https://doi.org/10.1007/s11665-021-06273-3.

[3] Saboori A, Aversa A, Marchese G, Biamino S, Lombardi M, Fino P. Microstructure and mechanical properties of AISI 316L produced by directed energy deposition-based additive manufacturing: a review. Appl Sci 2020;10. https://doi.org/10.3390/app10093310.

[4] Mosallanejad MH, Niroumand B, Aversa A, Saboori A. In-situ alloying in laser-based additive manufacturing processes: a critical review. J Alloys Compd 2021;872:159567. https://doi.org/10.1016/j.jallcom.2021.159567.

[5] de Formanoir C, Paggi U, Colebrants T, Thijs L, Li G, Vanmeensel K, et al. Increasing the productivity of laser powder bed fusion: influence of the hull-bulk strategy on part quality, microstructure and mechanical performance of Ti-6Al-4V. Addit Manuf 2020;33:101129. https://doi.org/10.1016/j.addma.2020.101129.

[6] Aristizabal M, Jamshidi P, Saboori A, Cox SC, Attallah MM. Laser powder bed fusion of a Zr-alloy: tensile properties and biocompatibility. Mater Lett 2020;259:126897. https://doi.org/10.1016/j.matlet.2019.126897.

[7] Bhavar V, Kattire P, Patil V, Khot S, Gujar K, Singh R. A review on powder bed fusion technology of metal additive manufacturing. 2014.

[8] Dadkhah M, Tulliani J-M, Saboori A, Iuliano L. Additive manufacturing of ceramics: advances, challenges, and outlook. J Eur Ceram Soc 2023;43:6635–64. https://doi.org/10.1016/j.jeurceramsoc.2023.07.033.

[9] Vyas C, Poologasundarampillai G, Hoyland J, Bartolo P. 3D printing of biocomposites for osteochondral tissue engineering. 2017. p. 261–302. https://doi.org/10.1016/B978-0-08-100752-5.00013-5.

[10] Cacace S, Semeraro Q. Improvement of SLM build rate of A357 alloy by optimizing fluence. J Manuf Process 2021;66:115–24. https://doi.org/10.1016/j.jmapro.2021.03.043.

[11] Dejene ND, Lemu HG. Current status and challenges of powder bed fusion-based metal additive manufacturing: literature review. Metals 2023;13. https://doi.org/10.3390/met13020424.

[12] Kan WH, Chiu LNS, Lim CVS, Zhu Y, Tian Y, Jiang D, et al. A critical review on the effects of process-induced porosity on the mechanical properties of alloys fabricated by laser powder bed fusion. J Mater Sci 2022;57:9818–65. https://doi.org/10.1007/s10853-022-06990-7.

[13] Cao S, Zou Y, Lim CVS, Wu X. Review of laser powder bed fusion (LPBF) fabricated Ti-6Al-4V: process, post-process treatment, microstructure, and property. Light Adv. Manuf. 2021;2:1. https://doi.org/10.37188/lam.2021.020.

[14] Viale V, Stavridis J, Salmi A, Bondioli F, Saboori A. Optimisation of downskin parameters to produce metallic parts via laser powder bed fusion process: an overview. Int J Adv Manuf Technol 2022;123:2159–82. https://doi.org/10.1007/s00170-022-10314-z.

[15] Gusarov AV, Grigoriev SN, Volosova MA, Melnik YA, Laskin A, Kotoban DV, et al. On productivity of laser additive manufacturing. J Mater Process Technol 2018;261:213–32. https://doi.org/10.1016/j.jmatprotec.2018.05.033.

[16] Leicht A, Fischer M, Klement U, Nyborg L, Hryha E. Increasing the productivity of laser powder bed fusion for stainless steel 316L through increased layer thickness. J Mater Eng Perform 2021;30:575–84. https://doi.org/10.1007/s11665-020-05334-3.

[17] Macoretta G, Bertini L, Monelli BD, Berto F. Productivity-oriented SLM process parameters effect on the fatigue strength of Inconel 718. Int J Fatig 2023;168:107384.

[18] Islam N, Schanz J, Kolb D, Riegel H. Improvement of surface quality and process area rate in selective laser melting by beam oscillation scan technique. J Mater Eng Perform 2021;30:5108–17. https://doi.org/10.1007/s11665-021-05665-9.

[19] Maamoun AH, Elbestawi M, Dosbaeva GK, Veldhuis SC. Thermal post-processing of AlSi10Mg parts produced by Selective Laser Melting using recycled powder. Addit Manuf 2018;21:234–47. https://doi.org/10.1016/j.addma.2018.03.014.

[20] Del Guercio G, Galati M, Saboori A. Innovative approach to evaluate the mechanical performance of Ti–6Al–4V lattice structures produced by electron beam melting process. Met Mater Int 2021;27:55–67. https://doi.org/10.1007/s12540-020-00745-2.

[21] Wang D, Wang H, Liu Z, Chen Z, Long Y, Zhang Y, et al. Influence mechanism of laser delay on internal defect and surface quality in stitching region of 316L stainless steel fabricated by dual-laser selective laser melting. J Manuf Process 2023;94:35–48. https://doi.org/10.1016/j.jmapro.2023.03.051.

[22] Subramanian R, Cwiok K, Kulkarni A. In: Ott EA, Andersson J, Sudbrack C, Bi Z, Bockenstedt K, Dempster I, et al., editors. Surface roughness of additively manufactured IN718 and H282 superalloys from multi-size and multi-laser machines BT - proceedings of the 10th international symposium on superalloy 718 and derivatives. Cham: Springer Nature Switzerland; 2023. p. 489–506.

[23] Liu Z, Yang Y, Song C, Zhou H, Chen Z, Liu Z, et al. The surface quality, microstructure and properties of SS316L using a variable area scan strategy during quad-laser large-scale powder bed fusion. Mater Sci Eng 2023;871:144450. https://doi.org/10.1016/j.msea.2022.144450.

[24] Mertens R, Dadbakhsh S, Van Humbeeck J, Kruth J-P. Application of base plate preheating during selective laser melting. Procedia CIRP 2018;74:5–11. https://doi.org/10.1016/j.procir.2018.08.002.

[25] Guan B, Yang X, Tang J, Qin L, Xu M, Yan Y, et al. Strategies to reduce pores and cracks of molybdenum fabricated by selective laser melting. Int J Refract Met Hard Mater 2023;112:106123. https://doi.org/10.1016/j.ijrmhm.2023.106123.

[26] Wilda N, Giedenbacher J, Huskic A. Material properties of AISI H10 (32CrMoV12-28) hot work tool steel processed by Laser Powder Bed Fusion with 200°C substrate preheating temperature. Procedia Comput Sci 2023;217:1008–17. https://doi.org/10.1016/j.procs.2022.12.299.

[27] Cheng B, Shrestha S, Chou K. Stress and deformation evaluations of scanning strategy effect in selective laser melting. Addit Manuf 2016;12:240–51. https://doi.org/10.1016/j.addma.2016.05.007.

[28] Jia Y, Zeng C, Xue J. Scanning strategy optimization for the selective laser melting additive manufacturing of Ti6Al4V. Eng Res Express 2023;5:15041. https://doi.org/10.1088/2631-8695/acbd12.

[29] Zhou L, Sun J, Bi X, Chen J, Chen W, Ren Y, et al. Effect of scanning strategies on the microstructure and mechanical properties of Ti–15Mo alloy fabricated by selective laser melting. Vacuum 2022;205. https://doi.org/10.1016/j.vacuum.2022.111454.

[30] Shi T, Sun J, Li J, Qian G, Hong Y. Machine learning based very-high-cycle fatigue life prediction of AlSi10Mg alloy fabricated by selective laser melting. Int J Fatig 2023;171:107585. https://doi.org/10.1016/j.ijfatigue.2023.107585.

[31] Agron DJS, Kim D-S, Lee J-M, Almendrala M. Smart monitoring program for selective laser melting 3D printing technology. In: 2023 IEEE 17th Int. Conf. Semant. Comput.; 2023. p. 337–40. https://doi.org/10.1109/ICSC56153.2023.00069.

[32] Wang T, Li S, Ren Z, Jia Y, Fu W, Guo M, et al. Microstructure characterization and mechanical property of Mg/Al laminated composite prepared by the novel approach: corrugated+ flat rolling (CFR). Metals 2019;9:690.

[33] Shi W, Han Y, Li J, Liu Y, Zhou Y, Lin Y. Investigation of the scanning strategy on the microstructure and tensile property of Ti6Al4V alloy fabricated by selective laser melting. Proc Inst Mech Eng Part C J Mech Eng Sci 2023;237:148–59. https://doi.org/10.1177/09544062221119938.

[34] Singh N, Hameed P, Ummethala R, Manivasagam G, Prashanth KG, Eckert J. Selective laser manufacturing of Ti-based alloys and composites: impact of process parameters, application trends, and future prospects. Mater Today Adv 2020;8:100097. https://doi.org/10.1016/j.mtadv.2020.100097.

[35] Mosallanejad MH, et al. Additive Manufacturing of Titanium Alloys: Processability, Properties, and Applications. Adv. Eng. Mater. 2023 https://doi.org/10.1002/adem.202301122.

[36] Eschner N, Weiser L, Häfner B, Lanza G. Development of an acoustic process monitoring system for selective laser melting (SLM), Solid Free. In: Fabr. 2018 Proc. 29th Annu. Int. Solid Free. Fabr. Symp. - An Addit. Manuf. Conf. SFF. 2020; 2018. p. 2097–117.

[37] Egan DS, Dowling DP. Influence of process parameters on the correlation between in-situ process monitoring data and the mechanical properties of Ti-6Al-4V non-stochastic cellular structures. Addit Manuf 2019;30:100890. https://doi.org/10.1016/j.addma.2019.100890.

[38] Zhou K, Han C. Metal powder-based additive manufacturing. John Wiley & Sons; 2023.

[39] Zhang Y, Hasan N, Middendorf J, Spears T, Smith T, Zhang F, et al. Correlating alloy Inconel 718 solidification microstructure to local thermal history using laser. In: Ott EA, Andersson J, Sudbrack C, Bi Z, Bockenstedt K, Dempster I, et al., editors. Powder bed fusion process monitoring BT - proceedings of the 10th international symposium on superalloy 718 and derivatives. Cham: Springer Nature Switzerland; 2023. p. 595–611.

[40] Conditions SLM. Understanding of excellent mechanical performance of 304L. 2023.

[41] Li X, Liu Y, Tan C, Zou Y. Porosity formation mechanisms, microstructure evolution and mechanical performance of AlMgScZr alloy fabricated by laser powder bed fusion: effect of hatch distance. J Manuf Process 2023;94:107–19. https://doi.org/10.1016/j.jmapro.2023.03.047.

[42] Toprak CB, Dogruer CU. Neuro-fuzzy modelling methods for relative density prediction of stainless steel 316L metal parts produced by additive manufacturing technique. J Mech Sci Technol 2023;37:107–18.

[43] Schnell N, Ferreira MP, Wegner J, Tillmann W, Kleszczynski S. Process strategy for crack-free production of diamond-reinforced metal matrix composites with minimal graphitization through laser powder bed fusion. Diam Relat Mater 2023;135:109788.
[44] Gibson I, Rosen DW, Stucker B. Additive manufacturing technologies: rapid prototyping to direct digital manufacturing. first ed. Springer Publishing Company, Incorporated; 2009.
[45] Behjat A, Shamanian M, Taherizadeh A, Lannunziata E, Bagherifard S, Gadalińska E, et al. Microstructure-electrochemical behavior relationship in post processed AISI316L stainless steel parts fabricated by laser powder bed fusion. J Mater Res Technol 2023;23:3294–311. https://doi.org/10.1016/j.jmrt.2023.01.229.
[46] Oliveira JP, LaLonde AD, Ma J. Processing parameters in laser powder bed fusion metal additive manufacturing. Mater Des 2020;193:1–12. https://doi.org/10.1016/j.matdes.2020.108762.
[47] Behjat A, Shamanian M, Taherizadeh A, Noori M, Lannunziata E, Iuliano L, et al. Enhanced surface properties and bioactivity of additively manufactured 316L stainless steel using different post-treatments. Mater Today Proc 2022. https://doi.org/10.1016/j.matpr.2022.09.019.
[48] Marrey M, Malekipour E, El-Mounayri H, Faierson EJ. A framework for optimizing process parameters in powder bed fusion (PBF) process using artificial neural network (ANN). Procedia Manuf 2019;34:505–15. https://doi.org/10.1016/j.promfg.2019.06.214.
[49] Roccetti Campagnoli M, Galati M, Saboori A. On the processability of copper components via powder-based additive manufacturing processes: potentials, challenges and feasible solutions. J Manuf Process 2021;72:320–37. https://doi.org/10.1016/j.jmapro.2021.10.038.
[50] Pragana J, Pombinha P, Duarte V, Rodrigues T, Oliveira JP, Braganca I, et al. Influence of processing parameters on the density of 316L stainless steel parts manufactured through laser powder bed fusion. Proc Inst Mech Eng Part B J Eng Manuf 2020;234:095440542091176. https://doi.org/10.1177/0954405420911768.
[51] Leicht A, Rashidi M, Klement U, Hryha E. Effect of process parameters on the microstructure, tensile strength and productivity of 316L parts produced by laser powder bed fusion. Mater Char 2020;159:110016. https://doi.org/10.1016/j.matchar.2019.110016.
[52] Keller C, Mokhtari M, Vieille B, Briatta H, Bernard P. Influence of a rescanning strategy with different laser powers on the microstructure and mechanical properties of Hastelloy X elaborated by powder bed fusion. Mater Sci Eng 2021;803:140474. https://doi.org/10.1016/j.msea.2020.140474.
[53] Montero-Sistiaga ML, Pourbabak S, Van Humbeeck J, Schryvers D, Vanmeensel K. Microstructure and mechanical properties of Hastelloy X produced by HP-SLM (high power selective laser melting). Mater Des 2019;165:107598. https://doi.org/10.1016/j.matdes.2019.107598.
[54] Yeung H, Lane B, Fox J. Part geometry and conduction-based laser power control for powder bed fusion additive manufacturing. Addit Manuf 2019;30:100844. https://doi.org/10.1016/j.addma.2019.100844.
[55] Meier H, Haberland C. Experimental studies on selective laser melting of metallic parts. Mater Werkst 2008;39:665–70. https://doi.org/10.1002/mawe.200800327.
[56] Liu J, Song Y, Chen C, Wang X, Li H, Zhou C, et al. Effect of scanning speed on the microstructure and mechanical behavior of 316L stainless steel fabricated by selective laser melting. Mater Des 2020;186:108355. https://doi.org/10.1016/j.matdes.2019.108355.
[57] Sadali M, Hassan M, Ahmad F, Yahaya H, Rasid ZA. Influence of selective laser melting scanning speed parameter on the surface morphology, surface roughness, and micropores for manufactured Ti6Al4V parts. J Mater Res 2020;35:1–11. https://doi.org/10.1557/jmr.2020.84.
[58] Yuan W, Chen H, Cheng T, Wei Q. Effects of laser scanning speeds on different states of the molten pool during selective laser melting: simulation and experiment. Mater Des 2020;189:108542. https://doi.org/10.1016/j.matdes.2020.108542.
[59] Badrossamay M, Yasa E, Van Vaerenbergh J, Kruth J-P. Improving productivity rate in SLM of commercial steel powders. Tech Pap Soc Manuf Eng 2009:1–13 [Article].
[60] Guan K, Wang Z, Gao M, Li X, Zeng X. Effects of processing parameters on tensile properties of selective laser melted 304 stainless steel. Mater Des 2013;50:581–6. https://doi.org/10.1016/j.matdes.2013.03.056.
[61] Calignano F, Cattano G, Manfredi D. Manufacturing of thin wall structures in AlSi10Mg alloy by laser powder bed fusion through process parameters. J Mater Process Technol 2018;255:773–83. https://doi.org/10.1016/j.jmatprotec.2018.01.029.
[62] Calignano F, Manfredi D, Ambrosio EP, Iuliano L, Fino P. Influence of process parameters on surface roughness of aluminum parts produced by DMLS. Int J Adv Manuf Technol 2013;67:2743–51. https://doi.org/10.1007/s00170-012-4688-9.
[63] Zhou YH, Li WP, Zhang L, Zhou SY, Jia X, Wang DW, et al. Selective laser melting of Ti–22Al–25Nb intermetallic: significant effects of hatch distance on microstructural features and mechanical properties. J Mater Process Technol 2020;276:116398. https://doi.org/10.1016/j.jmatprotec.2019.116398.
[64] Dong Z, Liu Y, Wen W, Ge J, Liang J. Effect of hatch spacing on melt pool and as-built quality during selective laser melting of stainless steel: modeling and experimental approaches. Materials 2018;12. https://doi.org/10.3390/ma12010050.
[65] Ehsan Saghaian S, Nematollahi M, Toker G, Hinojos A, Shayesteh Moghaddam N, Saedi S, et al. Effect of hatch spacing and laser power on microstructure, texture, and thermomechanical properties of laser powder bed fusion (L-PBF) additively manufactured NiTi. Opt Laser Technol 2022;149:107680. https://doi.org/10.1016/j.optlastec.2021.107680.
[66] Feng B, Wang C, Zhang Q, Ren Y, Cui L, Yang Q, et al. Effect of laser hatch spacing on the pore defects, phase transformation and properties of selective laser melting fabricated NiTi shape memory alloys. Mater Sci Eng 2022;840:142965. https://doi.org/10.1016/j.msea.2022.142965.
[67] Ramirez-Cedillo E, Uddin MJ, Sandoval-Robles JA, Mirshams RA, Ruiz-Huerta L, Rodriguez CA, et al. Process planning of L-PBF of AISI 316L for improving surface quality and relating part integrity with microstructural characteristics. Surf Coating Technol 2020;396:125956. https://doi.org/10.1016/j.surfcoat.2020.125956.
[68] Zhirnov I, Podrabinnik P, Tokbergenov M, Okunkova A, Smurov I. Optical monitoring and diagnostics of SLM processing for single track formation from Co-Cr alloy. Mater Sci Forum 2015;834:51–60. https://dx.doi.org/10.4028/www.scientific.net/MSF.834.51.
[69] Shi W, Liu Y, Shi X, Hou Y, Wang P, Song G. Beam diameter dependence of performance in thick-layer and high-power selective laser melting of Ti-6Al-4V. Materials 2018;11. https://doi.org/10.3390/ma11071237.
[70] Song Y, Sun Q, Guo K, Wang X, Liu J, Sun J. Effect of scanning strategies on the microstructure and mechanical behavior of 316L stainless steel fabricated by selective laser melting. Mater Sci Eng 2020;793:139879. https://doi.org/10.1016/j.msea.2020.139879.
[71] Zhao Y, Ding C, Chen H, Chen Y. Study on SLM forming process, residual stress and thermal fatigue of 24CrNiMo alloy steel. Mater (Basel, Switzerland) 2021;14. https://doi.org/10.3390/ma14164383.
[72] Nong X, Zhou XL, Wang YD, Yu L, Li JH. Effects of geometry, location, and direction on microstructure and mechanical properties of 15–5PH stainless steel fabricated by directed energy deposition. Mater Sci Eng 2021;821:141587. https://doi.org/10.1016/j.msea.2021.141587.
[73] Lu Y, Wu S, Gan Y, Huang T, Yang C, Junjie L, et al. Study on the microstructure, mechanical property and residual stress of SLM Inconel-718 alloy manufactured by differing island scanning strategy. Opt Laser Technol 2015;75:197–206. https://doi.org/10.1016/j.optlastec.2015.07.009.
[74] Wang Z, Xiao Z, Tse Y, Huang C, Zhang W. Optimization of processing parameters and establishment of a relationship between microstructure and mechanical properties of SLM titanium alloy. Opt Laser Technol 2019;112:159–67. https://doi.org/10.1016/j.optlastec.2018.11.014.
[75] Shi X, Yan C, Feng W, Zhang Y, Leng Z. Effect of high layer thickness on surface quality and defect behavior of Ti-6Al-4V fabricated by selective laser melting. Opt Laser Technol 2020;132:106471.
[76] Cutolo A, Neirinck B, Lietaert K, de Formanoir C, Van Hooreweder B. Influence of layer thickness and post-process treatments on the fatigue properties of CoCr scaffolds produced by laser powder bed fusion. Addit Manuf 2018;23:498–504. https://doi.org/10.1016/j.addma.2018.07.008.
[77] Goodridge R, Ziegelmeier S. 7 - powder bed fusion of polymers. In: Brandt M, editor. Laser addit. Manuf. Woodhead Publishing; 2017. p. 181–204. https://doi.org/10.1016/B978-0-08-100433-3.00007-5.
[78] Gorgin Karaji Z, Hedayati R, Pouran B, Apachitei I, Zadpoor AA. Effects of plasma electrolytic oxidation process on the mechanical properties of additively manufactured porous biomaterials. Mater Sci Eng C 2017;76:406–16. https://doi.org/10.1016/j.msec.2017.03.079.
[79] Mosallanejad MH, Sanaei S, Atapour M, Niroumand B, Iuliano L, Saboori A. Microstructure and corrosion properties of CP-Ti processed by laser powder bed fusion under similar energy densities. Acta Metall Sin (English Lett) 2022. https://doi.org/10.1007/s40195-022-01376-9.
[80] Buchbinder D, Schleifenbaum H, Heidrich S, Meiners W, Bültmann J. High power selective laser melting (HP SLM) of aluminum parts. Phys Procedia 2011;12:271–8.
[81] EOS 3D printing solutions, ([n.d.]).
[82] Wu Z, Tang G, Clark SJ, Meshkov A, Roychowdhury S, Gould B, et al. High frequency beam oscillation keyhole dynamics in laser melting revealed by in-situ x-ray imaging. Commun Mater 2023;4:5. https://doi.org/10.1038/s43246-023-00332-z.
[83] Alexander P, Allen S, Dutta D. Part orientation and build cost determination in layered manufacturing. Comput Des 1998;30:343–56.
[84] Hopkinson N, Dicknes P. Analysis of rapid manufacturing—using layer manufacturing processes for production. Proc Inst Mech Eng Part C J Mech Eng Sci 2003;217:31–9.
[85] Ruffo M, Hague R. Cost estimation for rapid manufacturing'simultaneous production of mixed components using laser sintering. Proc Inst Mech Eng Part B J Eng Manuf 2007;221:1585–91.
[86] Rickenbacher L, Spierings A, Wegener K. An integrated cost-model for selective laser melting (SLM). Rapid Prototyp J 2013;19:208–14. https://doi.org/10.1108/13552541311312201.
[87] Herzog D, Bartsch K, Bossen B. Productivity optimization of laser powder bed fusion by hot isostatic pressing. Addit Manuf 2020;36:101494. https://doi.org/10.1016/j.addma.2020.101494.
[88] https://www.eos.info/en, ([n.d.]).
[89] https://www.slm-solutions.com, ([n.d.]).
[90] https://www.ge.com/additive/who-we-are/concept-laser, ([n.d.]).
[91] Poprawe R, Hinke C, Meiners W, Schrage J, Bremen S, Merkt S. SLM production systems: recent developments in process development, machine concepts and component design. In: Brecher C, editor. Adv. Prod. Technol. Cham: Springer International Publishing; 2015. p. 49–65.
[92] Costabile G, Fera M, Fruggiero F, Lambiase A, Pham D. Cost models of additive manufacturing: a literature review. Int J Ind Eng Comput 2017;8:263–83.

[93] Atzeni E, Salmi A. Economics of additive manufacturing for end-useable metal parts. Int J Adv Manuf Technol 2012;62:1147–55. https://doi.org/10.1007/s00170-011-3878-1.

[94] https://it.airliquide.com/, https://ec.europa.eu/eurostat/statistics-explained/index.php?title=Electricity_price_statistics.

[95] Thomas DS, Gilbert SW. NIST special publication 1176. Gaithersburg, MD, USA: Natl. Inst. Stand. Technol.; 2014.

[96] Liu ZY, Li C, Fang XY, Guo YB. Energy consumption in additive manufacturing of metal parts. Procedia Manuf 2018;26:834–45. https://doi.org/10.1016/j.promfg.2018.07.104.

[97] Baumers M, Tuck C, Wildman R, Ashcroft I, Hague R. Energy inputs to additive manufacturing: does capacity utilization matter?. In: 2011 Int. Solid free. Fabr. Symp., University of Texas at Austin; 2011.

[98] Guo C, Li S, Shi S, Li X, Hu X, Zhu Q, et al. Effect of processing parameters on surface roughness, porosity and cracking of as-built IN738LC parts fabricated by laser powder bed fusion. J Mater Process Technol 2020;285:116788. https://doi.org/10.1016/j.jmatprotec.2020.116788.

[99] Ghanavati R, Lannunziata E, Norouzi E, Bagherifard S, Iuliano L, Saboori A. Design and development of SS316L-IN718 functionally graded materials via laser powder bed fusion. Mater Lett 2023;349:134793. https://doi.org/10.1016/j.matlet.2023.134793.

[100] Mosallanejad MH, Niroumand B, Aversa A, Manfredi D, Saboori A. Laser powder bed fusion in-situ alloying of Ti-5%Cu alloy: process-structure relationships. J Alloys Compd 2020:157558. https://doi.org/10.1016/j.jallcom.2020.157558.

[101] Behjat A, Shamanian M, Sadeghi F, Iuliano L, Saboori A. Additive manufacturing of a novel in-situ alloyed AISI316L-Cu stainless steel: microstructure and antibacterial properties. Mater Lett 2023:135363. https://doi.org/10.1016/j.matlet.2023.135363.

[102] Sun Z, Tan X, Tor SB, Yeong WY. Selective laser melting of stainless steel 316L with low porosity and high build rates. Mater Des 2016;104:197–204. https://doi.org/10.1016/j.matdes.2016.05.035.

[103] Saboori A, Toushekhah M, Aversa A, Lai M, Lombardi M, Biamino S, et al. Critical features in the microstructural analysis of AISI 316L produced by metal additive manufacturing. Metallogr Microstruct Anal 2020;9:92–6. https://doi.org/10.1007/s13632-019-00604-6.

[104] Eliasu A, Czekanski A, Boakye-Yiadom S. Effect of laser powder bed fusion parameters on the microstructural evolution and hardness of 316L stainless steel. Int J Adv Manuf Technol 2021;113:2651–69. https://doi.org/10.1007/s00170-021-06818-9.

[105] Sames WJ, List FA, Pannala S, Dehoff RR, Babu SS. The metallurgy and processing science of metal additive manufacturing. Int Mater Rev 2016;61:315–60.

[106] Jandaghi MR, Saboori A, Iuliano L, Pavese M. On the effect of rapid annealing on the microstructure and mechanical behavior of additively manufactured stainless steel by Laser Powder Bed Fusion. Mater Sci Eng 2021;828:142109. https://doi.org/10.1016/j.msea.2021.142109.

[107] Yakout M, Elbestawi MA, Veldhuis SC. Density and mechanical properties in selective laser melting of Invar 36 and stainless steel 316L. J Mater Process Technol 2019;266:397–420. https://doi.org/10.1016/j.jmatprotec.2018.11.006.

[108] Cherry JA, Davies HM, Mehmood S, Lavery NP, Brown SGR, Sienz J. Investigation into the effect of process parameters on microstructural and physical properties of 316L stainless steel parts by selective laser melting. Int J Adv Manuf Technol 2015;76:869–79. https://doi.org/10.1007/s00170-014-6297-2.

[109] Read N, Wang W, Essa K, Attallah MM. Selective laser melting of AlSi10Mg alloy: process optimisation and mechanical properties development. Mater Des 2015;65:417–24. https://doi.org/10.1016/j.matdes.2014.09.044.

[110] Brown C, Jacob G, Possolo A, Beauchamp C, Peltz M, Stoudt M, et al. The effects of laser powder bed fusion process parameters on material hardness and density for nickel alloy 625. https://doi.org/10.6028/NIST.AMS.100-19; 2018.

[111] Sun J, Yang Y, Wang D. Parametric optimization of selective laser melting for forming Ti6Al4V samples by Taguchi method. Opt Laser Technol 2013;49:118–24. https://doi.org/10.1016/j.optlastec.2012.12.002.

[112] Slotwinski J, Martin C, Johnson T. A survey of mechanical property variability of additively manufactured metals. 2021.

[113] Zheng Z, Wang L, Yan B. Effects of laser power on the microstructure and mechanical properties of 316L stainless steel prepared by selective laser melting. Int J Mod Phys B 2017;31:1744015. https://doi.org/10.1142/S0217979217440155.

[114] Yadroitsev I, Smurov I. Selective laser melting technology: from the single laser melted track stability to 3D parts of complex shape. Phys Procedia 2010;5:551–60. https://doi.org/10.1016/j.phpro.2010.08.083.

[115] Nguyen QB, Luu DN, Nai SML, Zhu Z, Chen Z, Wei J. The role of powder layer thickness on the quality of SLM printed parts. Arch Civ Mech Eng 2018;18:948–55. https://doi.org/10.1016/j.acme.2018.01.015.

[116] Shi X, Ma S, Liu C, Chen C, Wu Q, Chen X, et al. Performance of high layer thickness in selective laser melting of Ti6Al4V. Materials 2016;9. https://doi.org/10.3390/ma9120975.

[117] Sun S, Brandt M, Easton M. Powder bed fusion processes: an overview. Laser Addit Manuf 2017:55–77.

[118] Ulbricht A, Altenburg SJ, Sprengel M, Sommer K, Mohr G, Fritsch T, et al. Separation of the formation mechanisms of residual stresses in LPBF 316L. Metals 2020;10. https://doi.org/10.3390/met10091234.

[119] Dzukey G, Yang ke. Process parameter optimization for selective laser melting of 316L stainless steel material using taguchi's statistical design of experiment procedure. Int J Eng Technol 2019;11:6–13. https://doi.org/10.21817/ijet/2019/v11i1/191101014.

[120] Letenneur M, Kreitcberg A, Brailovski V. Optimization of laser powder bed fusion processing using a combination of melt pool modeling and design of experiment approaches: density control. J Manuf Mater Process. 2019;3. https://doi.org/10.3390/jmmp3010021.

Mohammad Taghian is currently a PhD student at the Department of Management and Production Engineering, Politecnico di Torino. His research interest is optimizing process parameters to produce metallic components via Additive Manufacturing.

Mohammadhossein Mosallanejad is currently a Postdoctoral Research Associate at the Department of Management and Production Engineering, Politecnico di Torino, and a member of the Integrated Additive Manufacturing Center at the same institution. Through his primary research focus on Additive Manufacturing of metallic components, he has authored several experimental and review papers on various aspects of AM, including process-structure properties and the development of novel alloys.

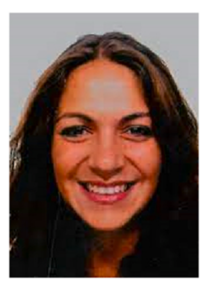

Erika Lannunziata is currently a PhD student at the Department of Management and Production Engineering, Politecnico di Torino. Her research interest is optimizing process parameters for producing metallic and polymeric components via Additive Manufacturing processes.

Giovanni del Greco got his M.Sc in Mechanical Engineering from Politecnico di Torino. His research in his M.Sc focused on the improvement of production rate in the laser powder bed fusion additive manufacturing of metallic materials.

Luca Iuliano is currently a Full Professor of manufacturing systems at the Department of Management and Production Engineering of the Politecnico di Torino (Italy), director of the Integrated Additive Manufacturing center at Politecnico di Torino and President of the Competence Center CIM 4.0 in Italy. He is the author and co-author of two Italian books on rapid prototyping and investment casting, and the author and coordinator of a handbook on foundry. He has published over 170 papers in academic journals and in national and international conference proceedings. From 2007, he was the coordinator of the First-level Master Course in "Manufacturing Systems" at Politecnico di Torino. From 2014, he has been a member of the technical-scientific committee of the ITS Foundation on Sustainable Aerospace/Mechatronics Mobility. From 2015, he has been the coordinator of the 2nd level Master Course in "Additive Manufacturing" at the Politecnico di Torino.

Abdollah Saboori is currently an Assistant Professor of Advance Materials Processing at the Department of Management and Production Engineering and a member of the Integrated Additive Manufacturing Center at Politecnico di Torino. He has published over 85 papers in academic journals and national and international conference proceedings. He is an editorial board member of several international journals and a scientific committee member of several international conferences in the field of metal Additive Manufacturing. His research deals with the correlation between the properties of metallic materials and metal additive manufacturing processes.